



*Supplement of*

## **Biological and dust aerosols as sources of ice-nucleating particles in the eastern Mediterranean: source apportionment, atmospheric processing and parameterization**

**Kunfeng Gao et al.**

*Correspondence to:* Kunfeng Gao (kunfeng.gao@epfl.ch) and Athanasios Nenes (athanasios.nenes@epfl.ch)

The copyright of individual parts of the supplement might differ from the article licence.

## **S1 Introduction**

This supplement document provides additional information and figures to support discussions in the main text.

S2 Particle size distribution used for FLEXPART model

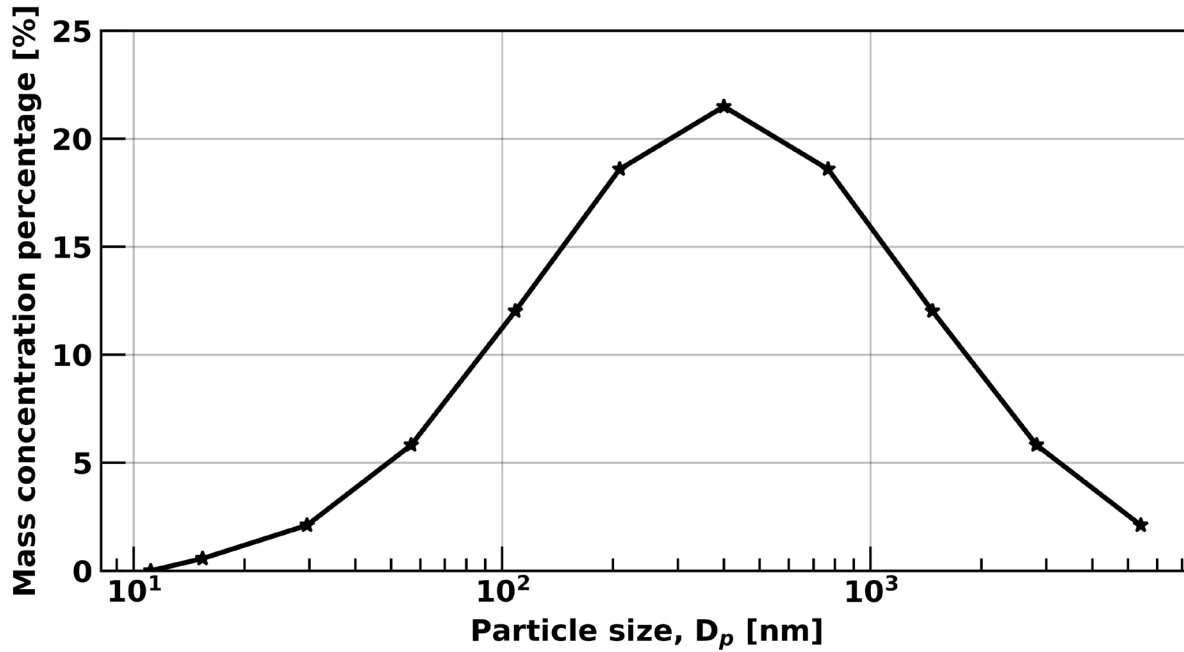
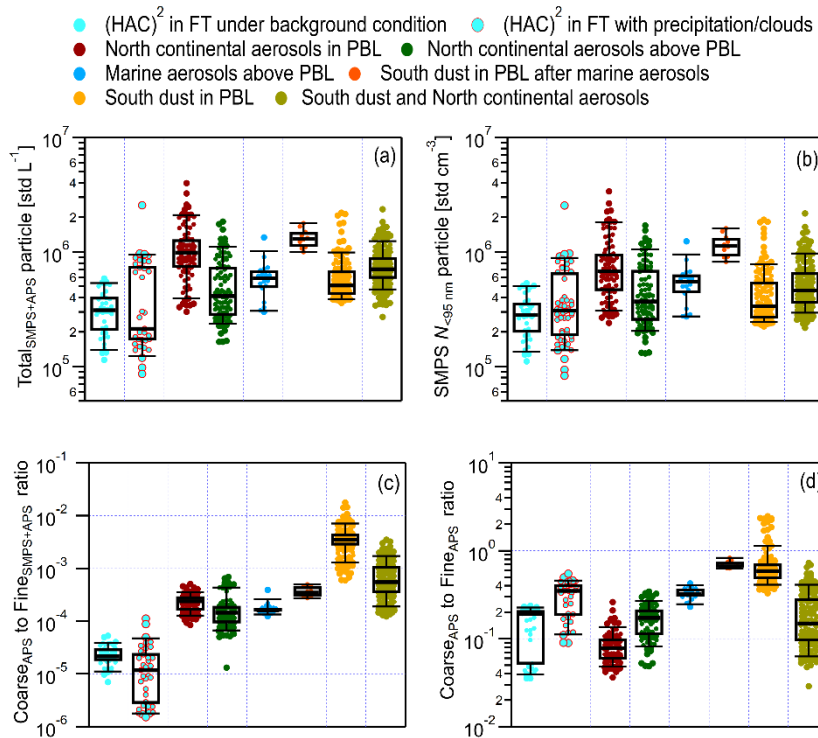


Figure S1. Particle size distribution in terms of particle mass concentration percentage for different size bins. The geometric mean diameter for the whole particle size distribution is 400 nm and the standard deviation is 3.3. The geometric mean diameter of each bin is indicated by the star marker.

30

Figure S1 provides the particle size distribution used as FLEXPART input.

### S3 Supplementary results on the characteristics of particles from different aerosol sources



35 **Figure S2. Box plots for particles in different size ranges from identified aerosol sources. (a) Total<sub>SMPS+APS</sub> particle (~0.01–20 μm) number concentration recorded by both SMPS and APS. (b) Number concentration of particles less than 95 nm measured by SMPS (SMPS  $N_{<95\text{nm}}$ ) at (HAC)<sup>2</sup>. (c) The ratio of Coarse<sub>APS</sub> particles (>1.0 μm, aerodynamic diameter) to Fine<sub>SMPS+APS</sub> particles (<1.0 μm, aerodynamic diameter). (d) The ratio of Coarse<sub>APS</sub> particles (>1.0 μm, aerodynamic diameter) to Fine<sub>APS</sub> particles (0.5–1.0 μm, aerodynamic diameter). The box shows the median line and the range between 25<sup>th</sup> and 75<sup>th</sup> quartiles. The lower and upper caps of the box indicate the 9<sup>th</sup> and 91<sup>th</sup> percentiles, respectively.**

40 Results in Fig. S2 support the discussions on Fig. 3 in the main text. Figure S2 shows particles in different size ranges for different aerosol sources, including Total<sub>SMPS+APS</sub> and SMPS  $N_{<95\text{ nm}}$  particle concentration, the ratio of Coarse<sub>APS</sub> to Fine<sub>SMPS+APS</sub> particle concentration and the ratio of Coarse<sub>APS</sub> to Fine<sub>APS</sub> particle concentration. The results provide more quantity details about the sizes of particles from different aerosol sources and help the discussion in Section 3.1 in the main text. Figure S2 shows that aerosol particle number concentration at (HAC)<sup>2</sup> spans a range of approximately two orders of magnitude from 10<sup>5</sup> to 10<sup>7</sup> std L<sup>-1</sup>. For (HAC)<sup>2</sup> in FT under background condition, aerosols have the lowest total particle number concentration, suggesting an overall clean atmosphere. Also, we note that total aerosols at (HAC)<sup>2</sup> in FT with precipitation/clouds have two subgroups (Fig. S2a), of which the upper group contains more SMPS  $N_{<95\text{nm}}$  particles compared to the lower group (Fig. S2a). Those fine particles in the upper group may be because of new particle formation facilitated by the presence of precipitation/clouds. Particles from North continental aerosols in PBL show an overall large Total<sub>SMPS+APS</sub> concentration (Fig. S2a) but show the lowest Coarse<sub>APS</sub> to Fine<sub>APS</sub> ratio (Fig. S2d), suggesting that fine particles dominate the

50

aerosol source. Above the PBL, North continental aerosols show decreased  $\text{Total}_{\text{SMPS}+\text{APS}}$  concentration while the  $\text{Coarse}_{\text{APS}}$  to  $\text{Fine}_{\text{APS}}$  ratio increases compared to the source in the PBL. The  $\text{Coarse}_{\text{APS}}$  to  $\text{Fine}_{\text{APS}}$  ratio of marine aerosols above PBL is larger than that of North continental aerosols above PBL (Fig. S2d), suggesting that sea salt particles may contribute to the coarse mode particles for marine aerosols (Khan et al., 2015). Aerosol sources containing dust particles generally show higher fraction of  $\text{Coarse}_{\text{APS}}$  particles (Fig. S2c and d) due to the enriched dust particles in coarse mode (Brunner et al., 2021).

- (HAC)<sup>2</sup> in FT under background condition
- (HAC)<sup>2</sup> in FT with precipitation/clouds
- North continental aerosols in PBL
- North continental aerosols above PBL
- Marine aerosols above PBL
- South dust in PBL after marine aerosols
- South dust in PBL
- South dust and North continental aerosols

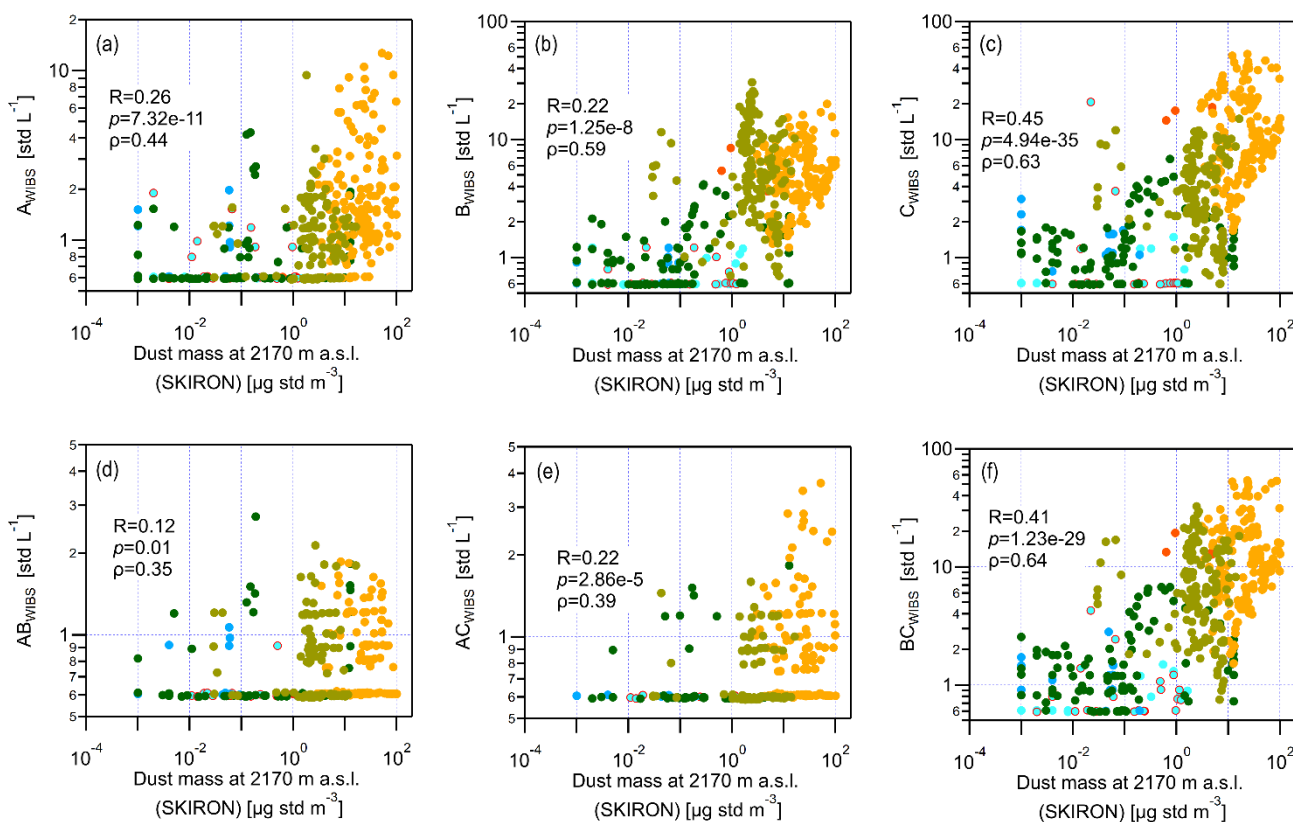


**Figure S3. The correlation between fluorescent particles in different WIBS channels and dust mass concentration estimated by SKIRON model at 2170 m a.s.l. (a)  $A_{\text{WIBS}}$ . (b)  $B_{\text{WIBS}}$ . (c)  $C_{\text{WIBS}}$ . (d)  $AB_{\text{WIBS}}$ . (e)  $AC_{\text{WIBS}}$ . (f)  $BC_{\text{WIBS}}$ . The Pearson correlation coefficient ( $R$ ) and corresponding  $p$  value calculated from F-test, and Spearman's rank coefficient ( $\rho$ ), are provided to evaluate the correlation between parameters on the  $x$ -axis and  $y$ -axis.**

Figure S3 shows that fluorescent particles in different aerosol sources, irrespective of the WIBS channel, generally increase with increasing dust mass concentration calculated by the SKIRON model at 2170 m a.s.l. ( $p > 0.05$ ). In particular,  $C_{\text{WIBS}}$  and  $BC_{\text{WIBS}}$  particles have a moderately linear correlation with the dust mass concentration ( $R > 0.4$ ), which is also significant ( $p < 0.05$ ). The results suggest that coarse-sized dust particles (also see Fig. 6 in the main text) may be relevant for fluorescent particles detected in  $C_{\text{WIBS}}$  and  $BC_{\text{WIBS}}$  channels.

- (HAC)<sup>2</sup> in FT under background condition
- (HAC)<sup>2</sup> in FT with precipitation/clouds
- North continental aerosols in PBL
- North continental aerosols above PBL
- Marine aerosols above PBL
- South dust in PBL after marine aerosols
- South dust in PBL
- South dust and North continental aerosols

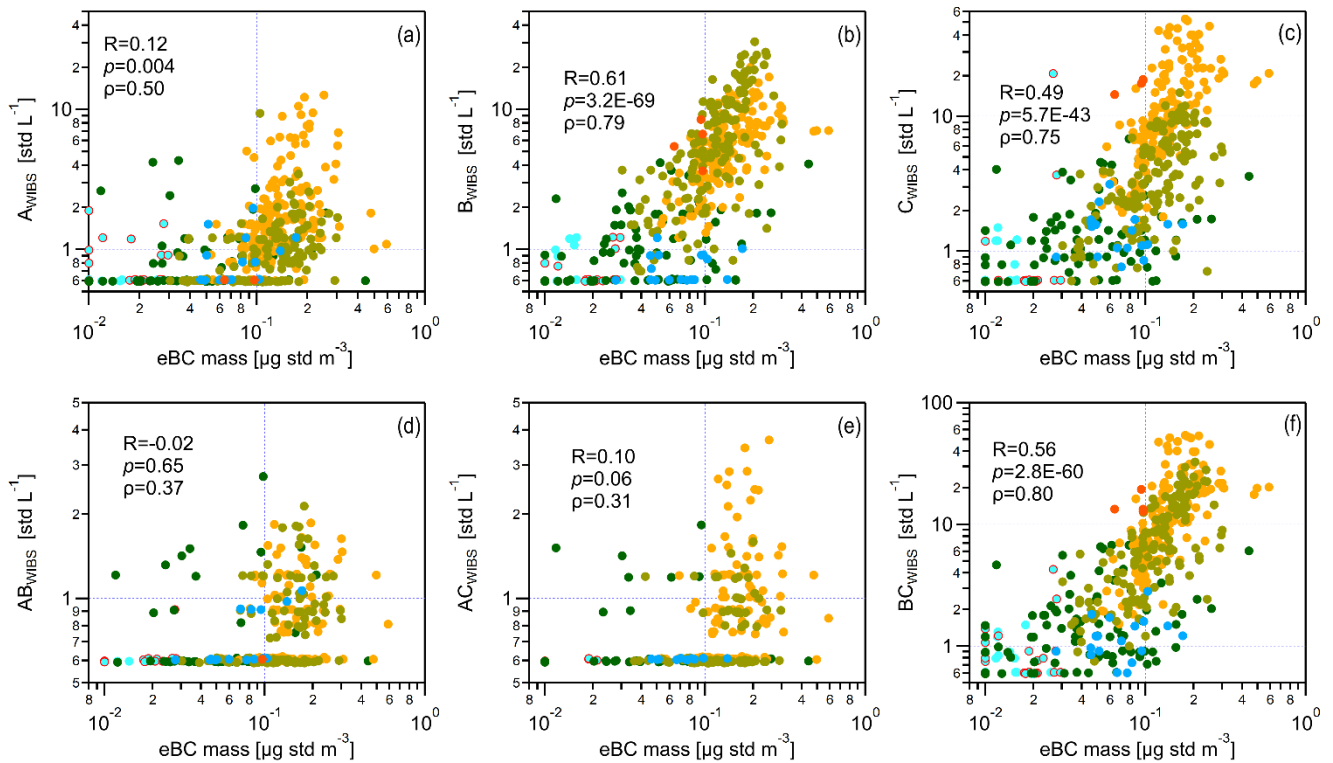


**Figure S4. The correlation between fluorescent particles in different WIBS channels and eBC mass concentration. (a)  $A_{\text{WIBS}}$ . (b)  $B_{\text{WIBS}}$ . (c)  $C_{\text{WIBS}}$ . (d)  $AB_{\text{WIBS}}$ . (e)  $AC_{\text{WIBS}}$ . (f)  $BC_{\text{WIBS}}$ . The Pearson correlation coefficient ( $R$ ) and corresponding  $p$  value calculated from F-test, and Spearman's rank coefficient ( $\rho$ ), are provided to evaluate the correlation between parameters on the  $x$ -axis and  $y$ -axis.**

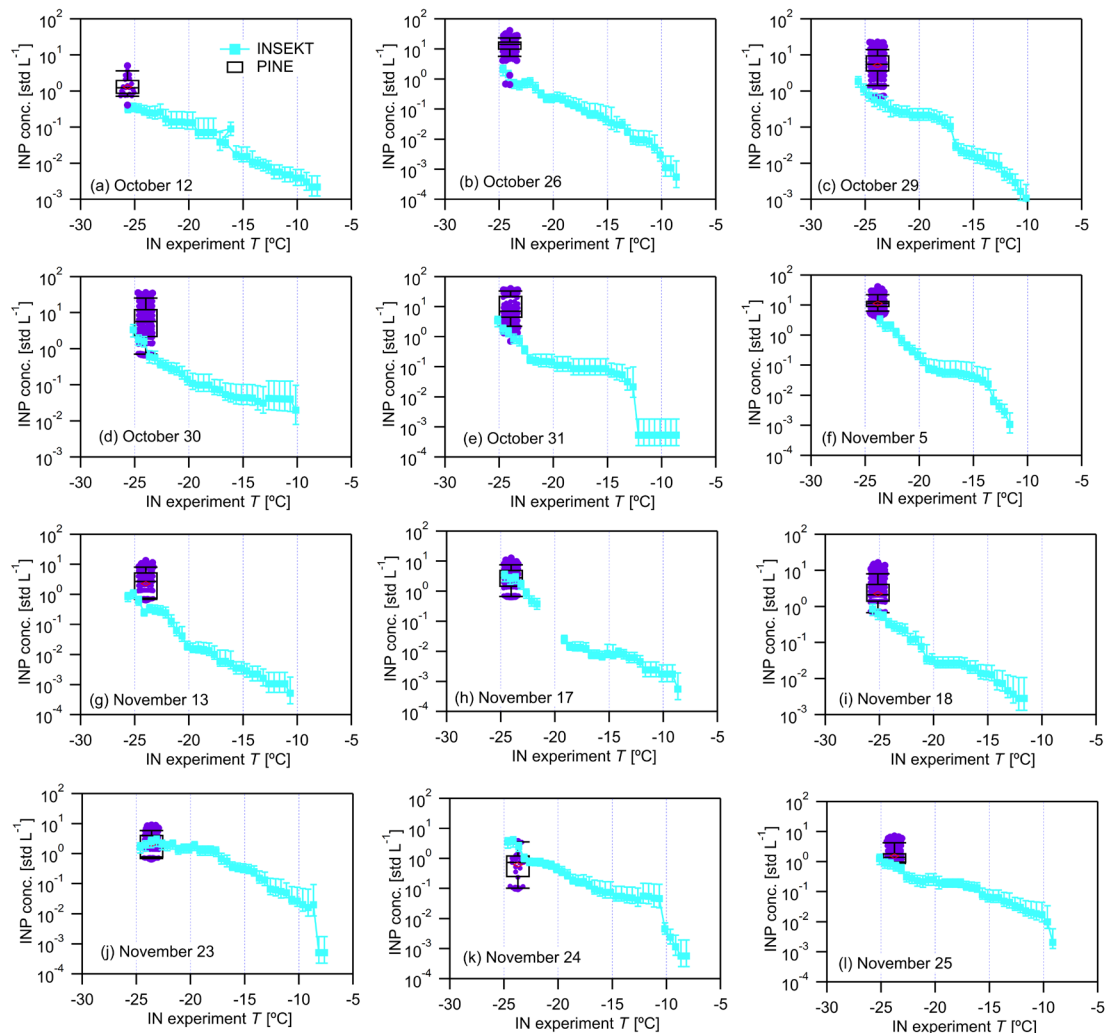
70

Figure S4 shows that different types of fluorescent particles in different aerosol sources generally increase with increasing eBC mass concentration ( $\rho > 0.3$ ). In particular,  $B_{\text{WIBS}}$ ,  $C_{\text{WIBS}}$  and  $BC_{\text{WIBS}}$  particles show a significant linear correlation with eBC mass concentration ( $R \geq 0.49$  and  $p < 0.05$ ) and the corresponding  $\rho$  value is larger than 0.75. The results suggest that small-sized anthropogenic carbonaceous aerosols (see Fig. 6 in the main text) may contribute to the fluorescence signals detected in

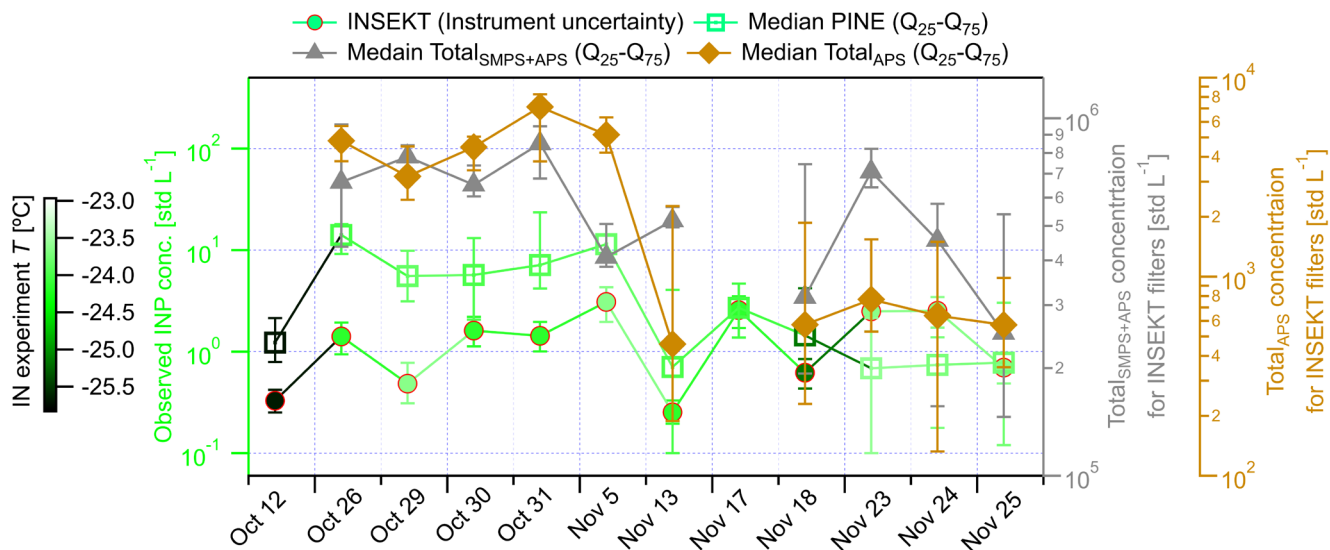
75

$B_{\text{WIBS}}$ ,  $C_{\text{WIBS}}$  and  $BC_{\text{WIBS}}$  channels.

## S4 The difference between INPs observed by PINE and INSEKT



80 **Figure S5. INPs observed by PINE and INSEKT on the same days when both instruments measure INPs at overlapped temperatures. INSEKT INP data are represented by blue line between points as a function of temperature. The error bar stands for the upper limit and lower limit concentrations measured by the instrument. Box plots show the INP concentration measured by PINE. PINE experiment temperatures have a standard deviation less than  $1.0^{\circ}\text{C}$ . Red diamonds are mean values of the PINE data.**



85 **Figure S6. INPs observed by PINE and INSEKT at the same temperature on those days when both types of INP data are available**  
 (on the left axis), and the average concentrations of Total<sub>SMPS+APS</sub> and Total<sub>APS</sub> particles for INSEKT filters (on the right axis).  
 INSEKT INP data are represented by round dots with a red boundary, with error bars indicating the upper limit and lower limit  
 90 concentrations measured by the instrument. Open squares are used for median INP values measured by PINE and the error bars  
 cover the Q<sub>25</sub>-Q<sub>75</sub> range. The color bar scales the ice nucleation (IN) experiment temperature (*T*). Triangles and diamonds indicate  
 the median values of Total<sub>SMPS+APS</sub> and Total<sub>APS</sub>, respectively.

Figures S5 and S6 compare the INP concentration results measured by online PINE and offline INSEKT techniques. The  
 results are used for discussing the results presented in Fig.8 in the main text. The presented PINE data in Figs. S5 and S6 are  
 from periods of INSEKT filter sampling when INSEKT experiments for the filter also address temperatures as low as PINE  
 experiments. The date indicated in both figures is the start date for the INSEKT filter sampling. Median values are presented  
 95 for PINE observations in Fig. S6 because it is reported that median INPs describe better for the INP results close to a lognormal  
 distribution (Brunner et al., 2021). Figures S5 and S6 show that PINE generally measures a higher INP concentration than  
 INSEKT. Barry et al. (2021) also reported higher INP concentrations from online experiments compared to offline filter  
 analysis. The lower INPs measured by INSEKT may be due to the decreasing particle collection efficiency during the filter  
 sampling for days with super high particle concentrations, like Saharan dust events. With increasing elapsed sampling time,  
 100 loaded particles may decrease the flow rate through the filter, impacting particle collection efficiency. In particular, PINE INPs  
 are higher than INSEKT INPs on some days, including October 12, 26, 29, 30, 31 and November 5 by more than a factor of 5  
 beyond the uncertainty range. This is because (HAC)<sup>2</sup> is basically in the PBL during the filter sampling time and the overall  
 aerosol particle concentration is much higher on those days than the other days. Thus, the filters might be over loaded on those  
 days and a substantial part of particles might not be collected onto the filter close to the end of the sampling. For the rest days  
 105 in both figures when (HAC)<sup>2</sup> is more in the FT with an overall lower particle number concentration, the two instruments report  
 similar INP results. In addition, aerosol particles deposited on filters may not be sufficiently collected in the liquid for INSEKT  
 experiments by washing. This can also be part of reason for the underestimation of INPs from INSEKT experiments. Last but

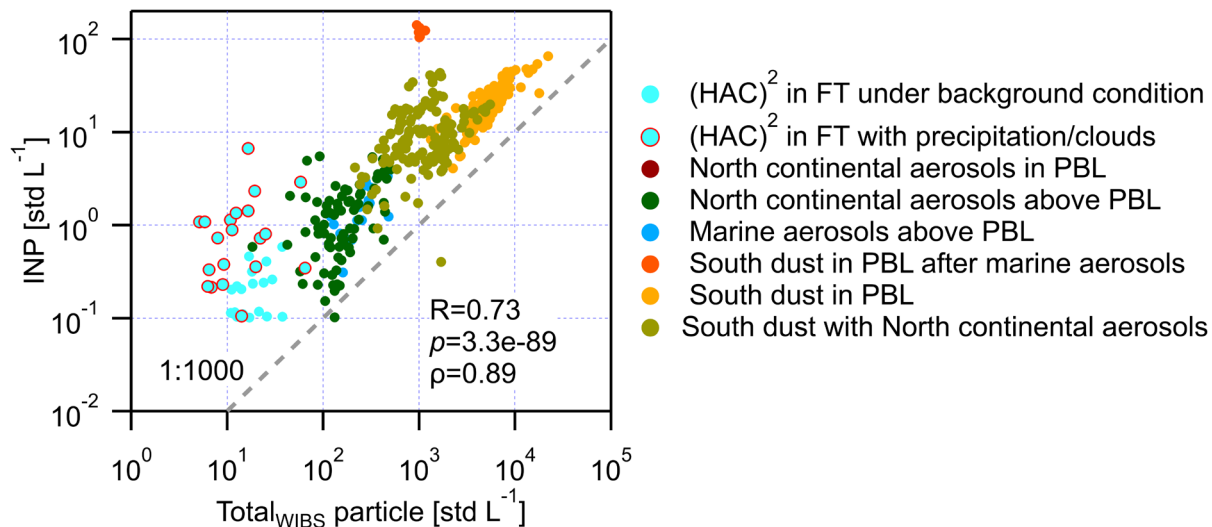


not least, we note that the concept and techniques of PINE and INSEKT are different. PINE measures INPs activating as ice in all ice nucleation mechanism whereas INSEKT only detects INPs in the immersion freezing mode.

110

## S5 The correlation between INP and Total<sub>WIBS</sub> concentration

Figure S7 shows that PINE INPs generally show a significant correlation with Total<sub>WIBS</sub> particle concentration and the Spearman's rank coefficient between the two is approximately 0.90. INPs from different individual sources show a correlation with Total<sub>WIBS</sub> similar to that of INPs and Coarse<sub>APS</sub> as presented in Fig. 9 and Table 2 in the main text.



115

Figure S7. Scatter plots showing the correlation between INP and Total<sub>WIBS</sub> concentrations. The Pearson correlation coefficient ( $R$ ) and corresponding  $p$  value calculated from F-test, and Spearman's rank coefficient ( $\rho$ ), are provided to statistically evaluate the correlation strength. The symbols are the same as those in Fig. S3.

120 **S6 The correlation between the ratio of INP to Total<sub>SMPS+APS</sub> concentration and the particle portioning in different aerosol sources**

Table S1 provides the Pearson correlation coefficient ( $R$ ) and corresponding  $p$  value calculated from F-test, and Spearman's rank coefficient ( $\rho$ ) to evaluate the correlation between the ratio of INP to Total<sub>SMPS+APS</sub> concentration (viewed as the average particle ice nucleation ability of the source) and different particle portioning conditions of the source, including Coarse<sub>APS</sub> to Total<sub>SMPS+APS</sub> ratio, Coarse<sub>APS</sub> to Total<sub>APS</sub> ratio, Fluow<sub>WIBS</sub> to Total<sub>SMPS+APS</sub> ratio and Fluow<sub>WIBS</sub> to Total<sub>WIBS</sub> ratio. The results in Table S1 supports the discussions on Fig. 10 in the main text.

125 **Table S1. The Pearson correlation coefficient ( $R$ ) and Spearman's rank coefficient ( $\rho$ ) for evaluating the relationship between the INP ratio (INP to Total<sub>SMPS+APS</sub> concentration ratio) of the source and the particle portioning condition of the source, including Coarse<sub>APS</sub> to Total<sub>SMPS+APS</sub> ratio, Coarse<sub>APS</sub> to Total<sub>APS</sub> ratio, Fluow<sub>WIBS</sub> to Total<sub>SMPS+APS</sub> ratio and Fluow<sub>WIBS</sub> to Total<sub>WIBS</sub> ratio. The  $p$  value of 0.05 from F-test for  $R$  was used to assess the significance of the relationship. Evaluated significant relationship is indicated in bold.**

INP sources	Coarse <sub>APS</sub> <sup>a</sup> to Total <sub>SMPS+APS</sub> <sup>b</sup>		Coarse <sub>APS</sub> to Fine <sub>APS</sub> <sup>c</sup>		Fluow <sub>WIBS</sub> <sup>d</sup> to Total <sub>SMPS+APS</sub>		Fluow <sub>WIBS</sub> to NonFluow <sub>WIBS</sub> <sup>e</sup>	
	$R$ ( $p$ )	$\rho$	$R$ ( $p$ )	$\rho$	$R$ ( $p$ )	$\rho$	$R$ ( $p$ )	$\rho$
(HAC) <sup>2</sup> in FT under background condition*	-0.12 (0.48)	-0.10	<b>-0.47</b> ( <b>0.005</b> )	-0.36	0.01 (0.97)	0.15	-0.18 (0.50)	-0.27
(HAC) <sup>2</sup> in FT with Precipitation/Clouds	<b>0.35</b> ( <b>0.04</b> )	0.57	-0.05 (0.79)	-0.12	0.20 (0.35)	0.51	0.34 (0.12)	0.49
North continental aerosols in PBL	<b>0.54</b> ( <b>2.4e-7</b> )	0.66	-0.17 (0.12)	-0.24	NA <sup>f</sup>	NA	NA	NA
North continental aerosols above PBL	<b>0.64</b> ( <b>2.3e-11</b> )	0.47	-0.003 (0.97)	0.09	<b>0.54</b> ( <b>8.5e-8</b> )	0.58	0.02 (0.88)	0.16
Marine air masses above PBL	0.10 (0.69)	0.41	-0.25 (0.31)	-0.29	0.36 (0.14)	0.19	0.06 (0.80)	0.11
South dust in PBL after marine aerosols	0.27 (0.60)	0.37	-0.09 (0.87)	-0.09	-0.05 (0.93)	-0.14	-0.31 (0.55)	-0.43
South dust in PBL	<b>0.89</b> ( <b>1.8e-50</b> )	0.90	<b>0.30</b> ( <b>3.3e-4</b> )	0.49	<b>0.60</b> ( <b>2.0e-15</b> )	0.56	-0.19 (0.09)	-0.16
South dust with North continental aerosols	<b>0.23</b> ( <b>0.002</b> )	0.37	0.04 (0.55)	0.24	<b>0.53</b> ( <b>2.1e-11</b> )	0.35	<b>0.28</b> ( <b>7.7e-4</b> )	0.07
All observations	<b>0.85</b> ( <b>9.4e-225</b> )	0.78	<b>0.50</b> ( <b>5.9e-54</b> )	0.29	<b>0.75</b> ( <b>9.4e-93</b> )	0.81	<b>-0.23</b> ( <b>1.1e-7</b> )	-0.55

<sup>a</sup> Coarse particle (>1.0  $\mu\text{m}$ ) number concentration measured by APS

<sup>b</sup> Total particle (0.01–20.0  $\mu\text{m}$ ) number concentration measured by both SMPS and APS

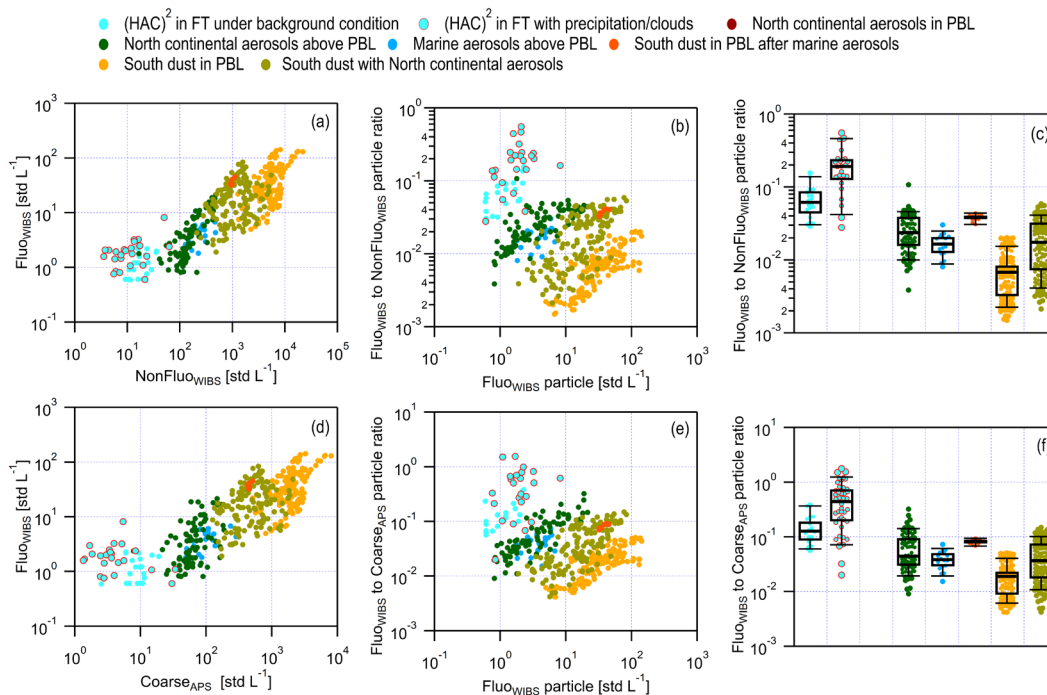
<sup>c</sup> Fine particle (<1.0  $\mu\text{m}$ ) number concentration measured by APS

135 <sup>d</sup> Number concentration of particles showing fluorescence in any one of WIBS fluorescent channels

<sup>e</sup> Nonfluorescent particle (0.5–30.0  $\mu\text{m}$  in optical size) number concentration measured by WIBS

<sup>f</sup> Data not available

## S7 The correlation of Fluow<sub>WIBS</sub> particles with NonFluow<sub>WIBS</sub> and Coarse<sub>APS</sub> particles



140

**Figure S8. Scatter and box plots for the correlation of Fluow<sub>WIBS</sub> particles with NonFluow<sub>WIBS</sub> and Coarse<sub>APS</sub> particles. (a) Scatter plots for Fluow<sub>WIBS</sub> and NonFluow<sub>WIBS</sub> (the difference between Total<sub>WIBS</sub> and Fluow<sub>WIBS</sub>) particle concentrations. (b) The Fluow<sub>WIBS</sub> to NonFluow<sub>WIBS</sub> ratio of different aerosol sources as a function of Fluow<sub>WIBS</sub>. (c) Box plots for the Fluow<sub>WIBS</sub> to NonFluow<sub>WIBS</sub> ratio of different aerosol sources. (d) Scatter plots for Fluow<sub>WIBS</sub> and Coarse<sub>APS</sub> particle concentrations. (e) The Fluow<sub>WIBS</sub> to Coarse<sub>APS</sub> ratio of different aerosol sources as a function of Coarse<sub>APS</sub>. (f) Box plots for the Fluow<sub>WIBS</sub> to Coarse<sub>APS</sub> ratio of different aerosol sources.**

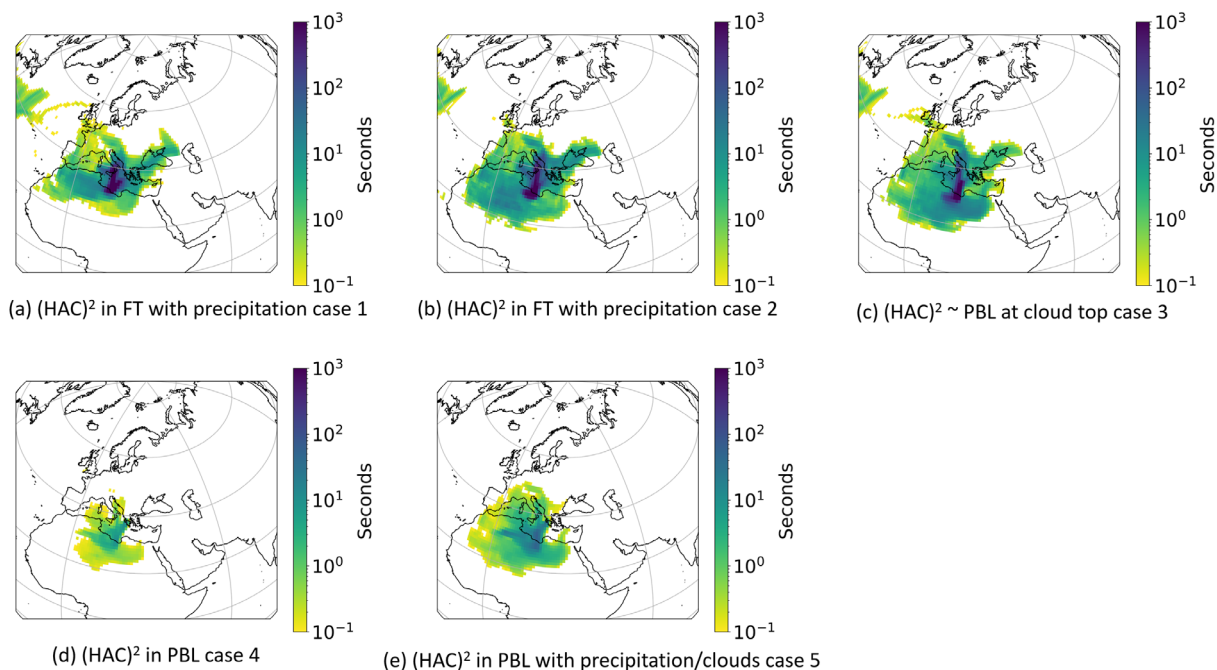
145

Figure S8a and d respectively show that Fluow<sub>WIBS</sub> particles generally increases with increasing NonFluow<sub>WIBS</sub> and Coarse<sub>APS</sub> particles in different aerosol sources. However, Figure S8b and e respectively show that Fluow<sub>WIBS</sub> to NonFluow<sub>WIBS</sub> ratio and Fluow<sub>WIBS</sub> to Coarse<sub>APS</sub> ratio generally decrease with increasing Fluow<sub>WIBS</sub> particle concentration in different sources. The results suggest that Fluow<sub>WIBS</sub> particle changes in different sources follow a similar trend with the change of Coarse<sub>APS</sub> and NonFluow<sub>WIBS</sub> particles. However, Fluow<sub>WIBS</sub> to Coarse<sub>APS</sub> ratio is generally larger than Fluow<sub>WIBS</sub> to NonFluow<sub>WIBS</sub> ratio. The results presented in this section support the discussion on Fig. 10e in the main text.

150

## S8 The source apportionment and particles properties of aerosols observed on November 23 for the case study

155 Figure S9 shows that North continental aerosols dominate the particle sources for  $(\text{HAC})^2$  on November 23 and South dust may play a minor role in the particle sources. Importantly, the sources of air masses generally do not change throughout the day. Thus, it allows to investigate the only effect of precipitation/clouds and  $(\text{HAC})^2$  position *wrt.* PBL on INPs and aerosol properties, excluding the influences from aerosol source changes. The air mass back trajectories in Fig. S10 further demonstrate that aerosols over  $(\text{HAC})^2$  on November 23 does not change substantially over the day. The particle size distribution results of  
 160 different cases in Fig. S11 show that the overall aerosol particle concentration is increasing over the day when  $(\text{HAC})^2$  is more involved in the PBL, in particular for accumulation mode and coarse mode particles. These results can also be seen from Fig. S12a and b. Furthermore, Figure S12 shows that the ultrafine mode and Aitken mode particles (Fig. S12c),  $\text{Fluo}_{\text{WIBS}}$  less than  $10.0 \mu\text{m}$  (Figs. S12d and S13),  $\text{ABC}_{\text{WIBS}}$  between  $2.0\text{--}8.0 \mu\text{m}$  (Figs. S12e and S13) and eBC mass (Fig. S12f), are increasing when  $(\text{HAC})^2$  is more influenced by aerosols from the PBL. Those results suggest that the concentrations of fine particles and  
 165 biological particles (possibly  $\text{ABC}_{\text{WIBS}}$  particles), as well as eBC particles on November 23, are driven by the local emissions close to  $(\text{HAC})^2$ . Notably, the increase in fine mode particles for the last period (case 5) classified on November 23 suggests the effect of precipitation/clouds on new particle formation when  $(\text{HAC})^2$  is in PBL with available sources. In addition, the decreased concentrations in  $\text{Fluo}_{\text{WIBS}}$  (Fig. S12d),  $\text{ABC}_{\text{WIBS}}$  (Fig. S12e) and eBC mass (Fig. S12f) for case 5 with the influence of precipitation/clouds at  $(\text{HAC})^2$  in PBL suggest the wet removal effects of precipitation/clouds.



170

**Figure S9.** FLEXPART 10 day backward results showing the footprints of aerosols around  $(\text{HAC})^2$  in the range from 0 to 500 m a.g.l. during different periods on November 23, 2021 for the case study discussed in main text Section 3.3. (a)  $(\text{HAC})^2$  in FT with precipitation case 1 from 00:00 to 04:00. (b)  $(\text{HAC})^2$  in FT with precipitation case 2 from 05:00 to 09:00. (c)  $(\text{HAC})^2$  around PBL

and close to cloud top from 10:00 to 15:00. (d)  $(\text{HAC})^2$  in PBL from 15:30 to 18:00. (e)  $(\text{HAC})^2$  in PBL with clouds (precipitation below  $(\text{HAC})^2$ ) from 19:00 to 24:00. Aerosol particles are released during the period for each scenario to calculate the FELXPART results.

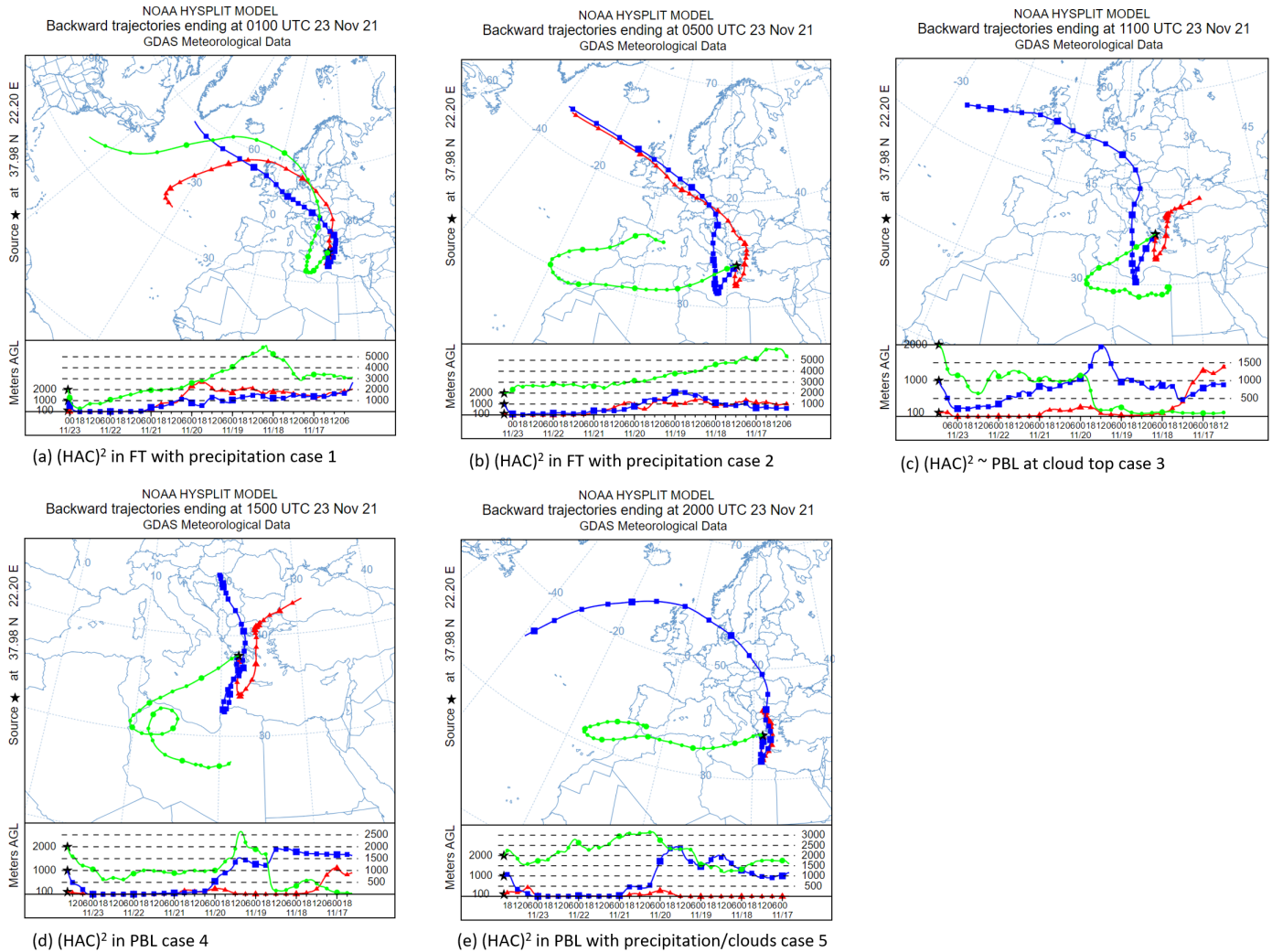
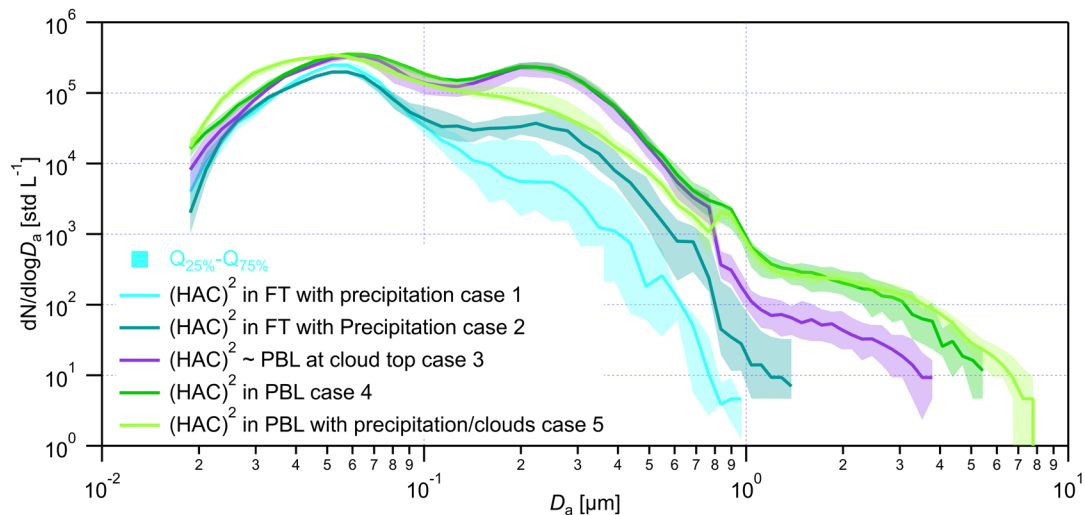
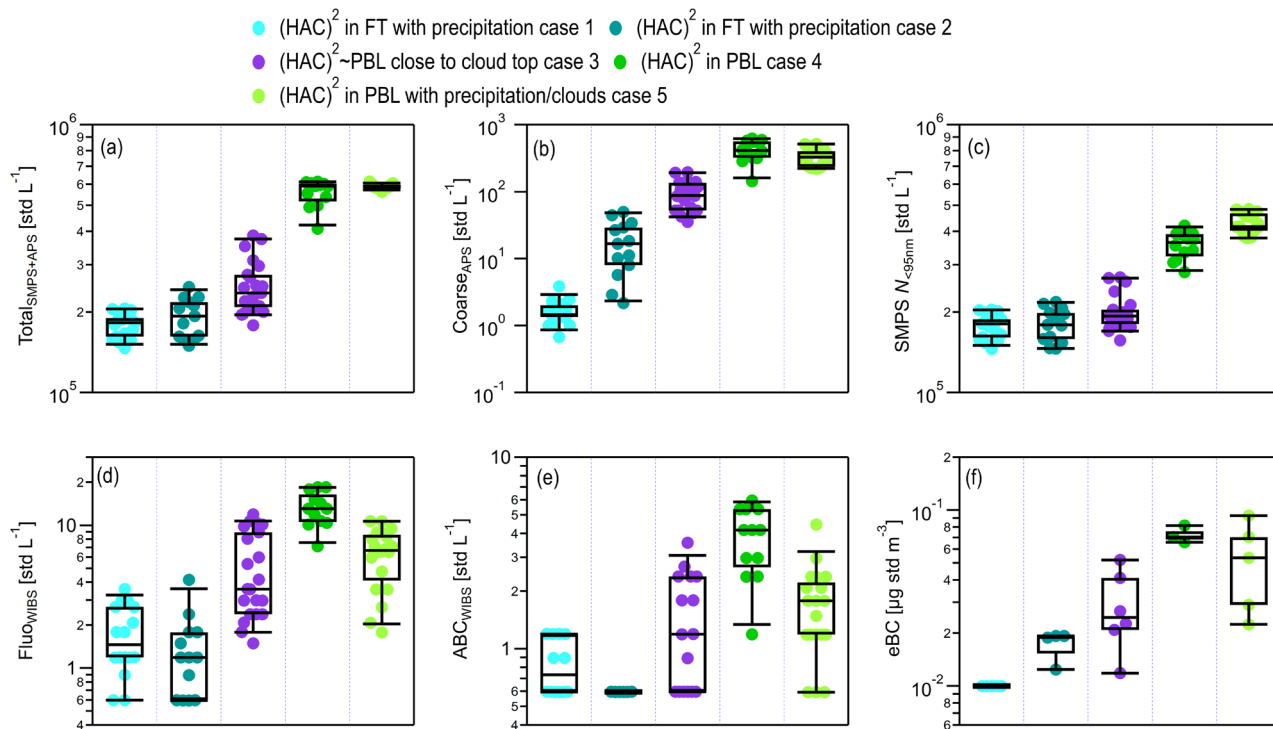


**Figure S10.** Seven day back trajectories for air masses around  $(\text{HAC})^2$  during the period for different scenarios of the case study on November 23 discussed in the main text Section 3.3. (a)  $(\text{HAC})^2$  in FT with precipitation case 1 from 00:00 to 04:00. (b)  $(\text{HAC})^2$  in FT with precipitation case 2 from 05:00 to 09:00. (c)  $(\text{HAC})^2$  around PBL and close to cloud top from 10:00 to 15:00. (d)  $(\text{HAC})^2$  in PBL from 15:30 to 18:00. (e)  $(\text{HAC})^2$  in PBL with clouds (precipitation below  $(\text{HAC})^2$ ) from 19:00 to 24:00. Aerosol particles are released during the period for each scenario to calculate the FELXPART results.



180 **Figure S11. Combined size distribution of particles measured by SMPS (10–800 nm in mobility diameter) and APS (0.5–20 μm in aerodynamic diameter) aerosols observed in different scenarios on November 23. SMPS mobility diameter was converted to APS aerodynamic diameter using the method introduced in Khlystov et al. (2004). The solid line is the median of the aerosol source particle size distribution. The shading area shows the 25<sup>th</sup> to 75<sup>th</sup> percentiles of the particle size distribution of each INP source.**



185 **Figure S12. Box plots for the aerosol property results of different scenarios classified on November 23. Identified scenarios are indicated in the legend. (a) Total<sub>SMPS+APS</sub> particle concentration. (b) Coarse<sub>APS</sub> particle concentration. (c) SMPS  $N_{<95\text{nm}}$  particle concentration. (d) Flu<sub>OwIBS</sub> particle concentration. (e) ABC<sub>wIBS</sub> particle concentration. (f) eBC mass concentration.**

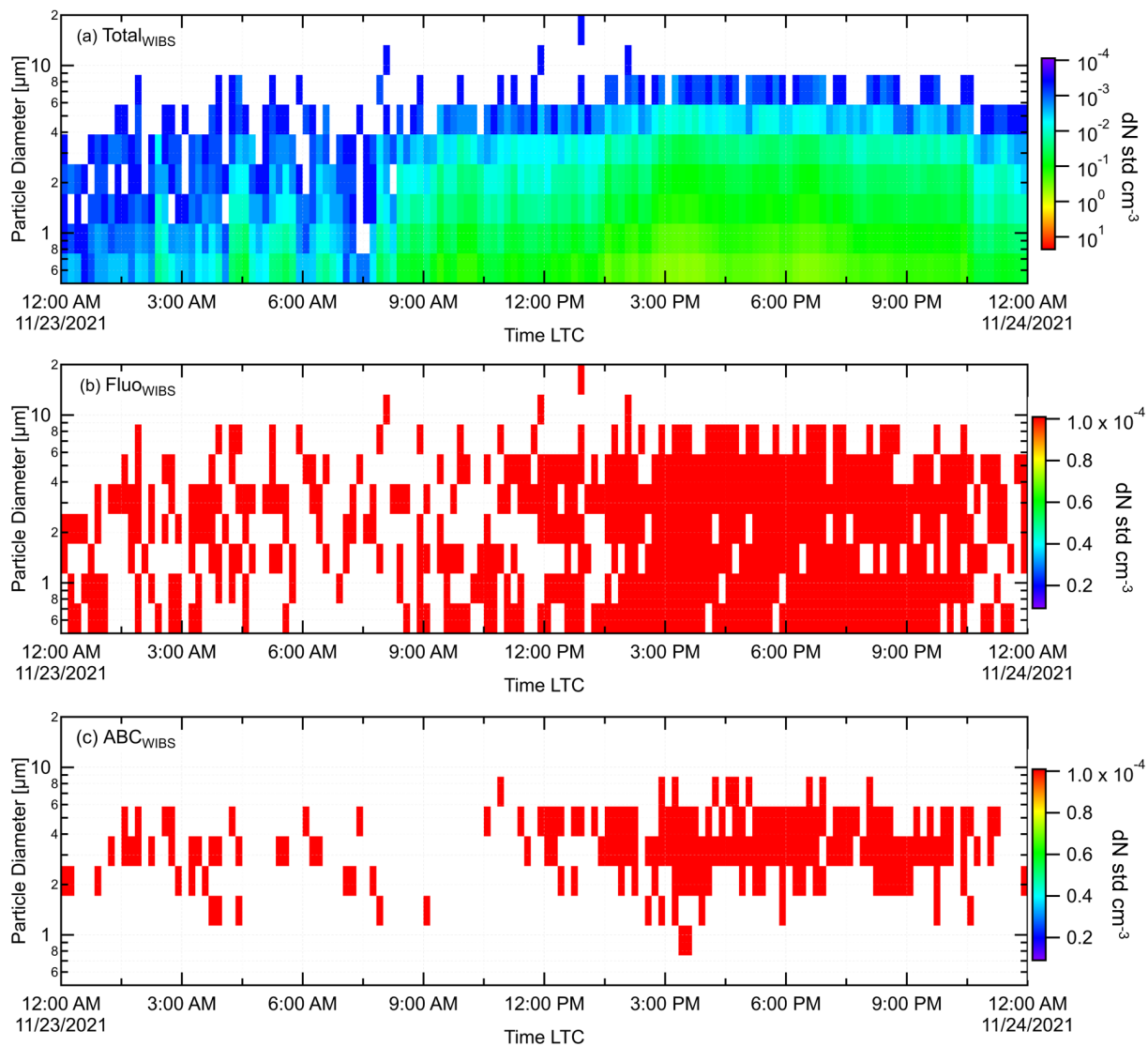


Figure S13. The size distribution for Total<sub>WIBS</sub> (a), Fluor<sub>WIBS</sub> (b) and ABC<sub>WIBS</sub> (c) recorded by WIBS on November 23.



190 **S9 The predictability of INP parameterizations reported from the literature for INPs originated from different sources**  
**when both APS and WIBS data are available**

This section provides results to evaluate the performance of different INP parameterizations from the literature to predict INPs from different sources. The results support the discussions on the results in Fig. 13 in Section 3.4.1. Note that the source apportionment for INSEKT INPs was conducted only when the whole INSEKT filter sampling period fitted in a period of  
195 classified aerosol source.

Nonlinear regression with robust fitting option was used to calculate parameters for each proposed parameterization. Bisquare robust fitting was used for the regression model function to minimize a weighted sum of squares (to minimize the effect of outliers – and advantage over the least-squares approach). Weighted least square options were also suggested in the recent literature for INP parameterizations (Li et al., 2022). Also, fitted parameters were calculated with the error term normally  
200 distributed with mean 0 and standard deviation  $\leq 0.1$ .

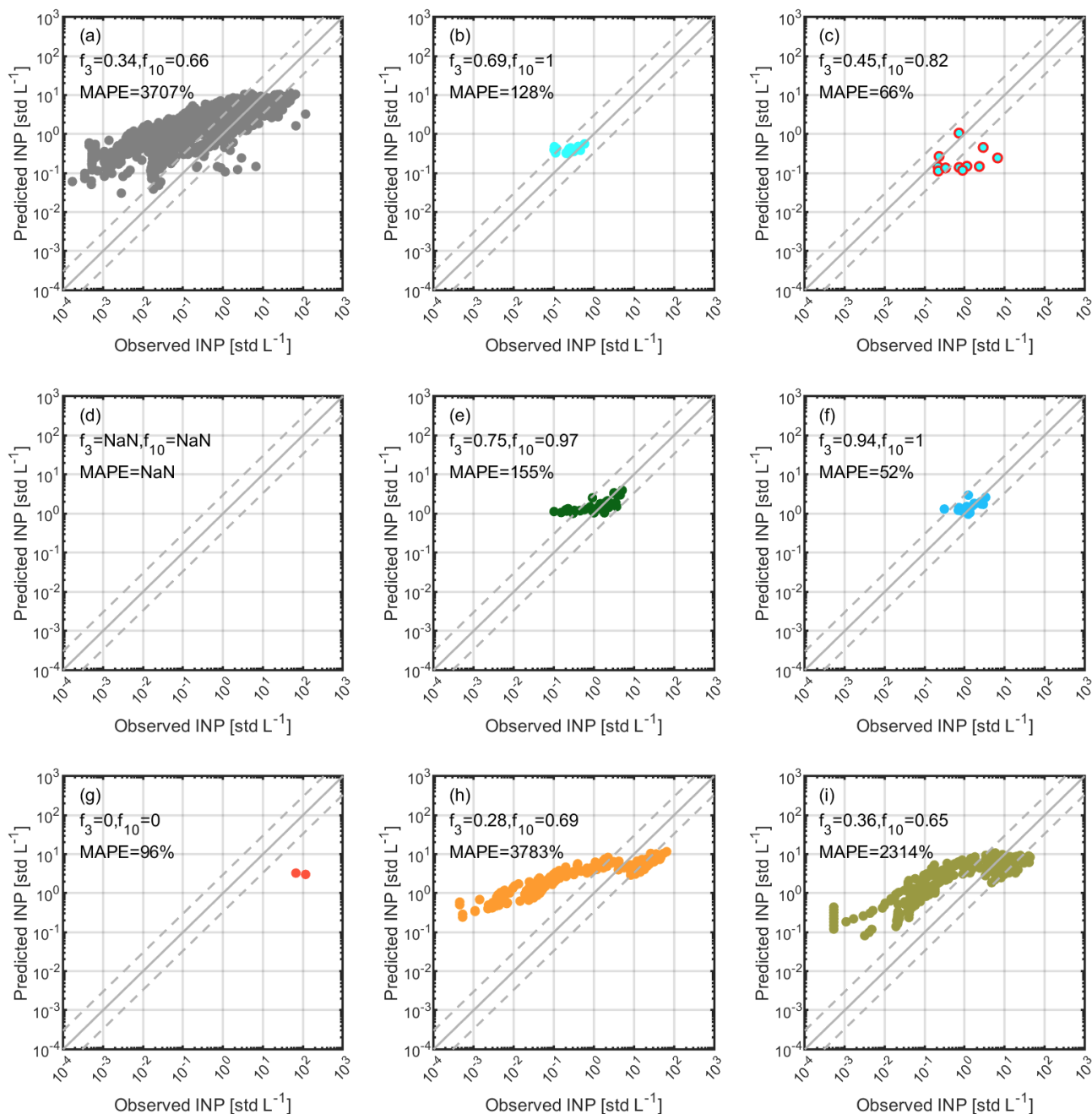
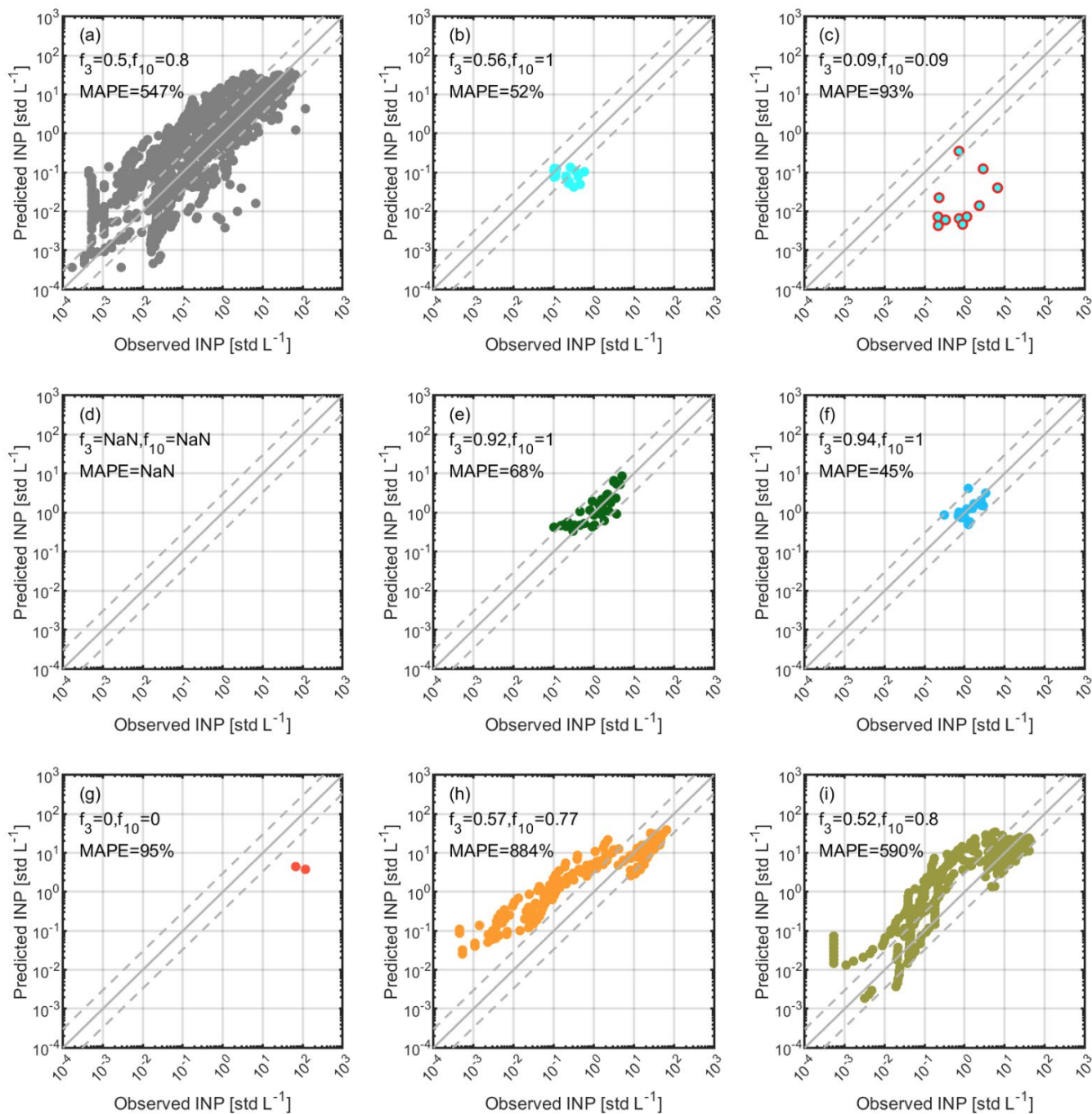
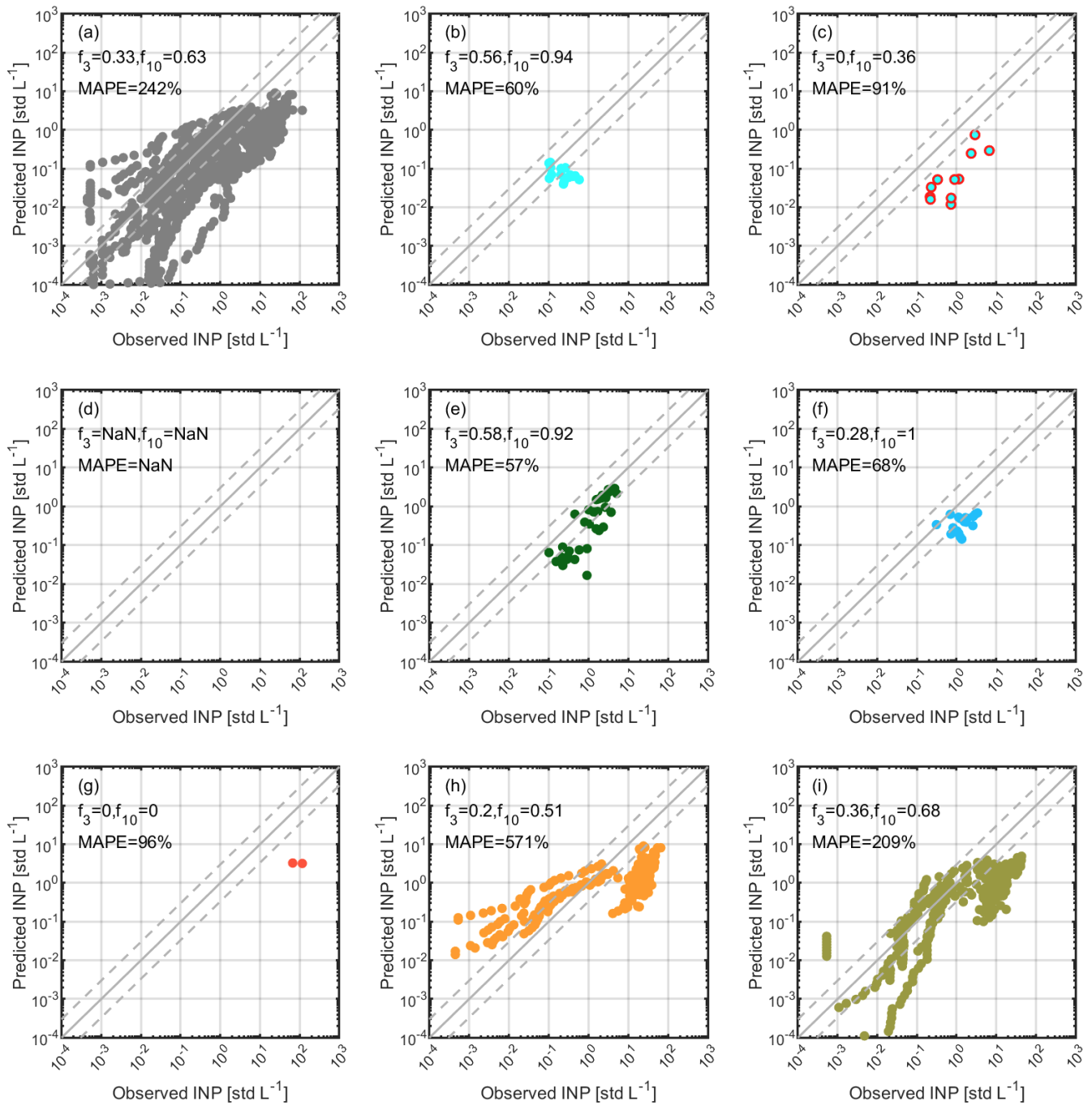


**Figure S14.** The predictability of DeMott2010 for INPs observed at (HAC)<sup>2</sup> from different sources when both APS and WIBS data are available. (a) All observations when both APS and WIBS data are available. (b) (HAC)<sup>2</sup> in FT under background condition. (c) (HAC)<sup>2</sup> in FT with precipitation/clouds. (d) North continental aerosols in PBL. No WIBS data. (e) North continental aerosols above PBL. (f) Marine aerosols above PBL. (g) South dust in PBL after marine aerosols. (h) South dust in PBL. (i) South dust with North continental aerosols. Note that the sum of sub-datasets from panel (b) to (i) is smaller than the dataset presented in panel (a) because INP source apportionment is not available for all observations.

205

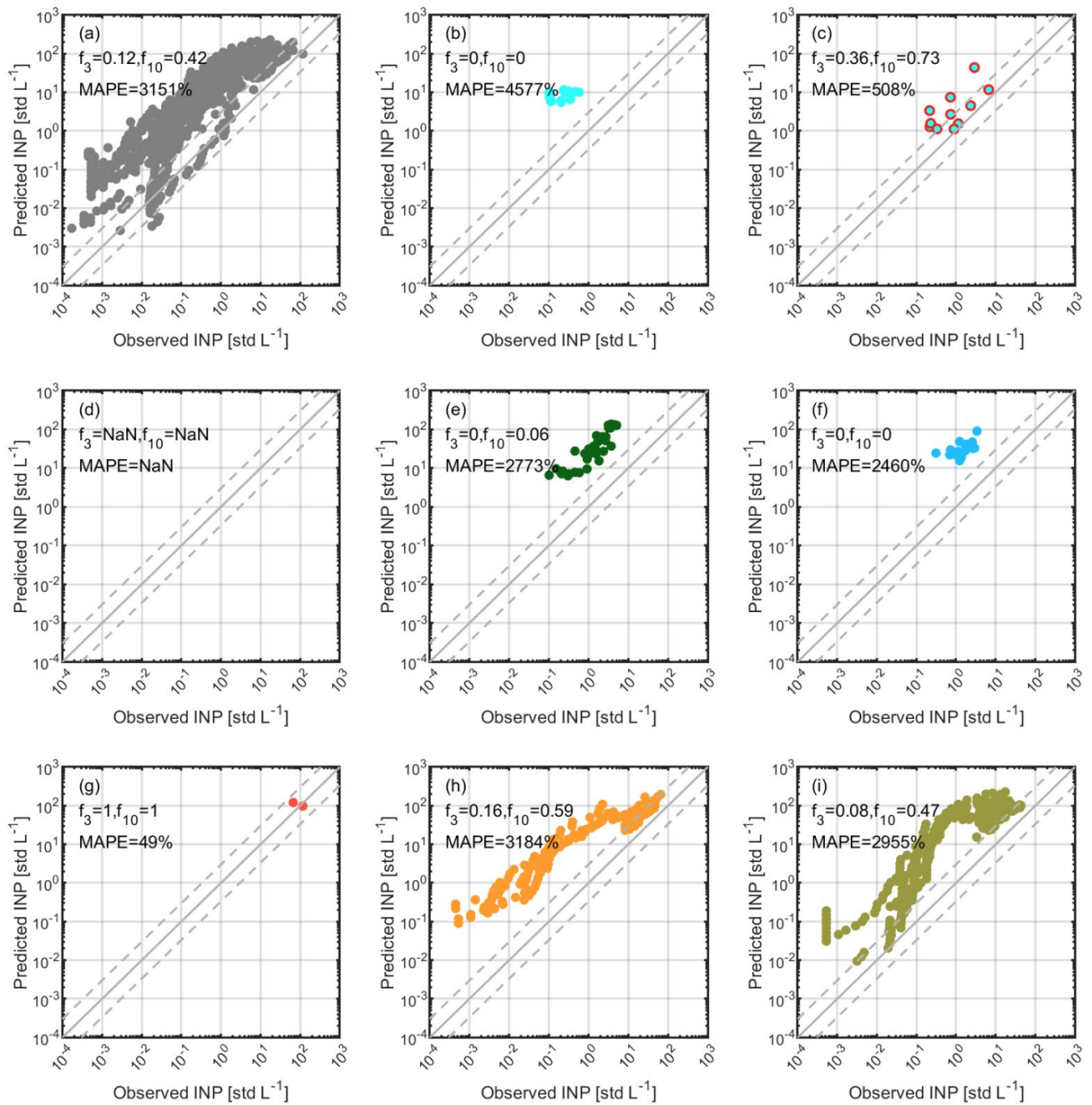


210 **Figure S15.** The same as Fig. S14 but for evaluating the predictability of DeMott2015. We note that the gap for observed INPs in panel (h) may be due to the lower estimation of INPs by INSEKT compared to PINE (see Section S3). Note that the sum of sub-datasets from panel (b) to (i) is smaller than the dataset presented in panel (a) because INP source apportionment is not available for all observations.



215

**Figure S16.** The same as Fig. S14 but for evaluating the predictability of Tobo2013. Note that the sum of sub-datasets from panel (b) to (i) is smaller than the dataset presented in panel (a) because INP source apportionment is not available for all observations.



220

**Figure S 17.** The same as Fig. S14 but for evaluating the predictability of Niemand2012. Note that the sum of sub-datasets from panel (b) to (i) is smaller than the dataset presented in panel (a) because INP source apportionment is not available for all observations.

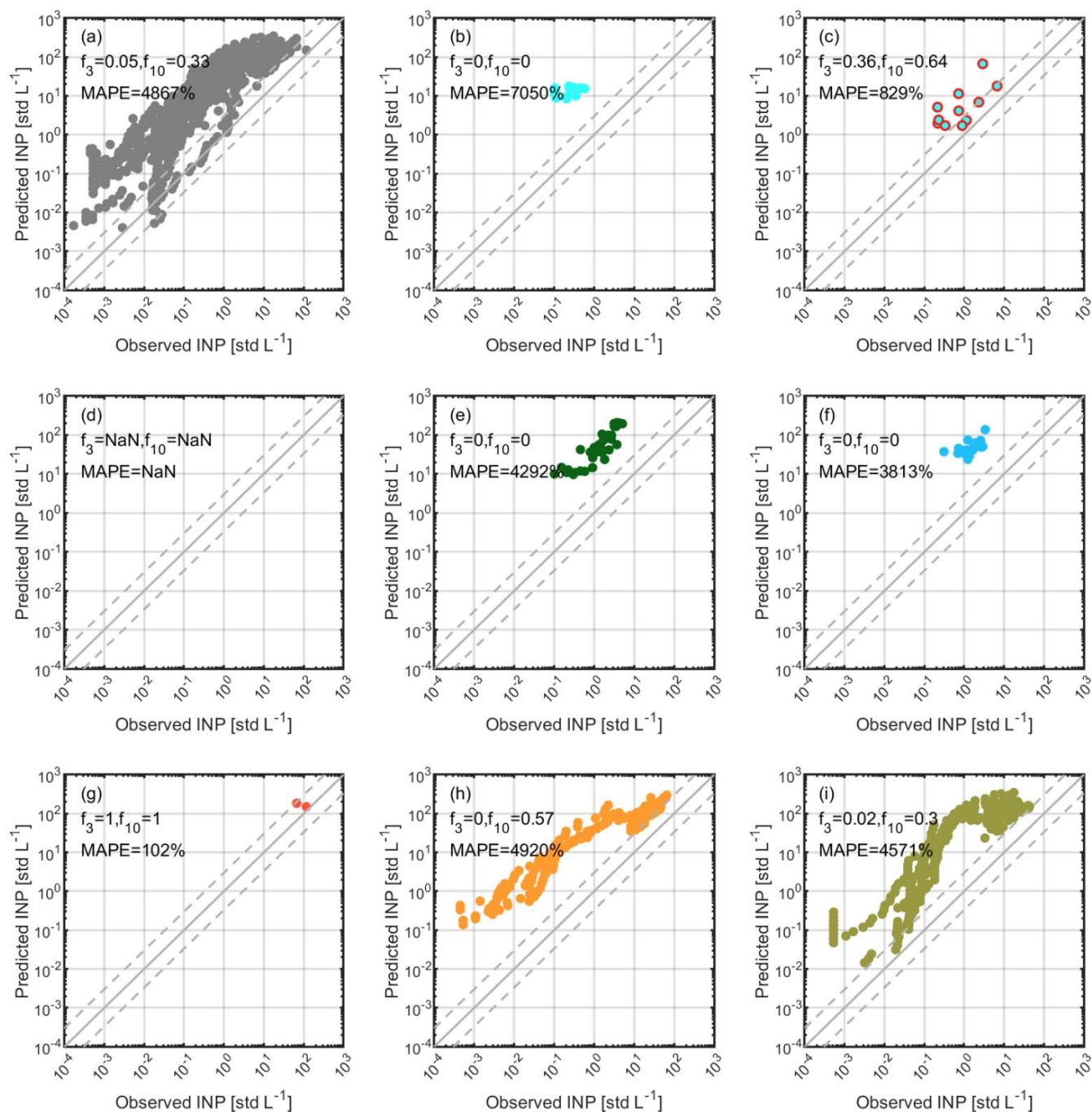


**Figure S18.** The same as Fig. S14 but for evaluating the predictability of Ullrich2017. Note that the sum of sub-datasets from panel (b) to (i) is smaller than the dataset presented in panel (a) because INP source apportionment is not available for all observations.

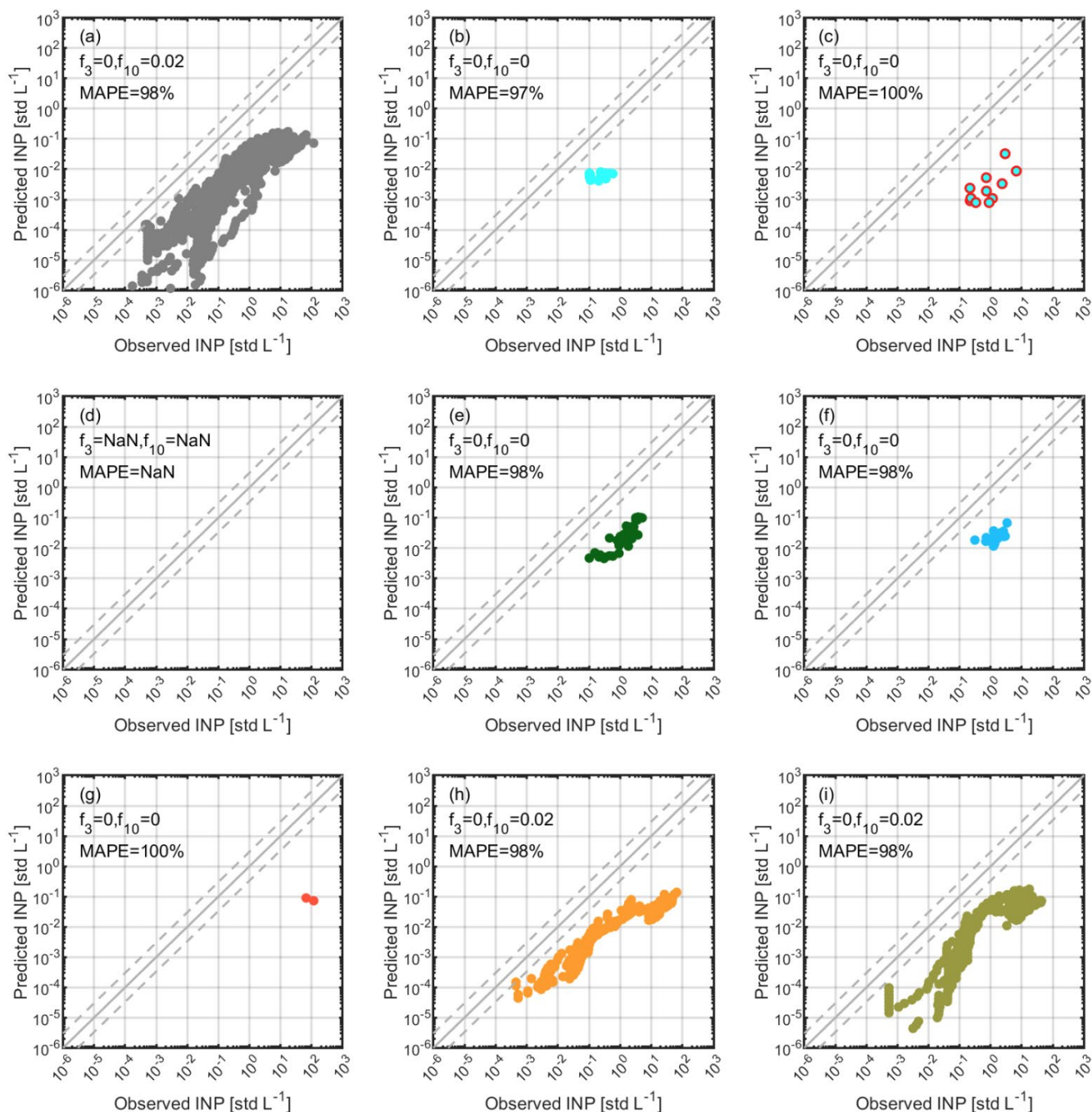


**Figure S19.** The same as Fig. S14 but for evaluating the predictability of McCluskey2018. Note that the sum of sub-datasets from panel (b) to (i) is smaller than the dataset presented in panel (a) because INP source apportionment is not available for all observations.

235 **S10 The predictability of INP parameterizations proposed in this study for INPs originated from different sources when both APS and WIBS data are available**

This section provides results to evaluate the performance of different INP parameterizations proposed in this study to predict INPs from different sources. The results support the discussions in Fig. 14 in Section 3.4.2. Note that the lower predictability for INPs from the source of South dust in PBL after marine aerosols may be due to the very limited observations. Note that 240 the source apportionment for INSEKT INPs was conducted only when the whole INSEKT filter sampling period fitted in a period of classified aerosol source.



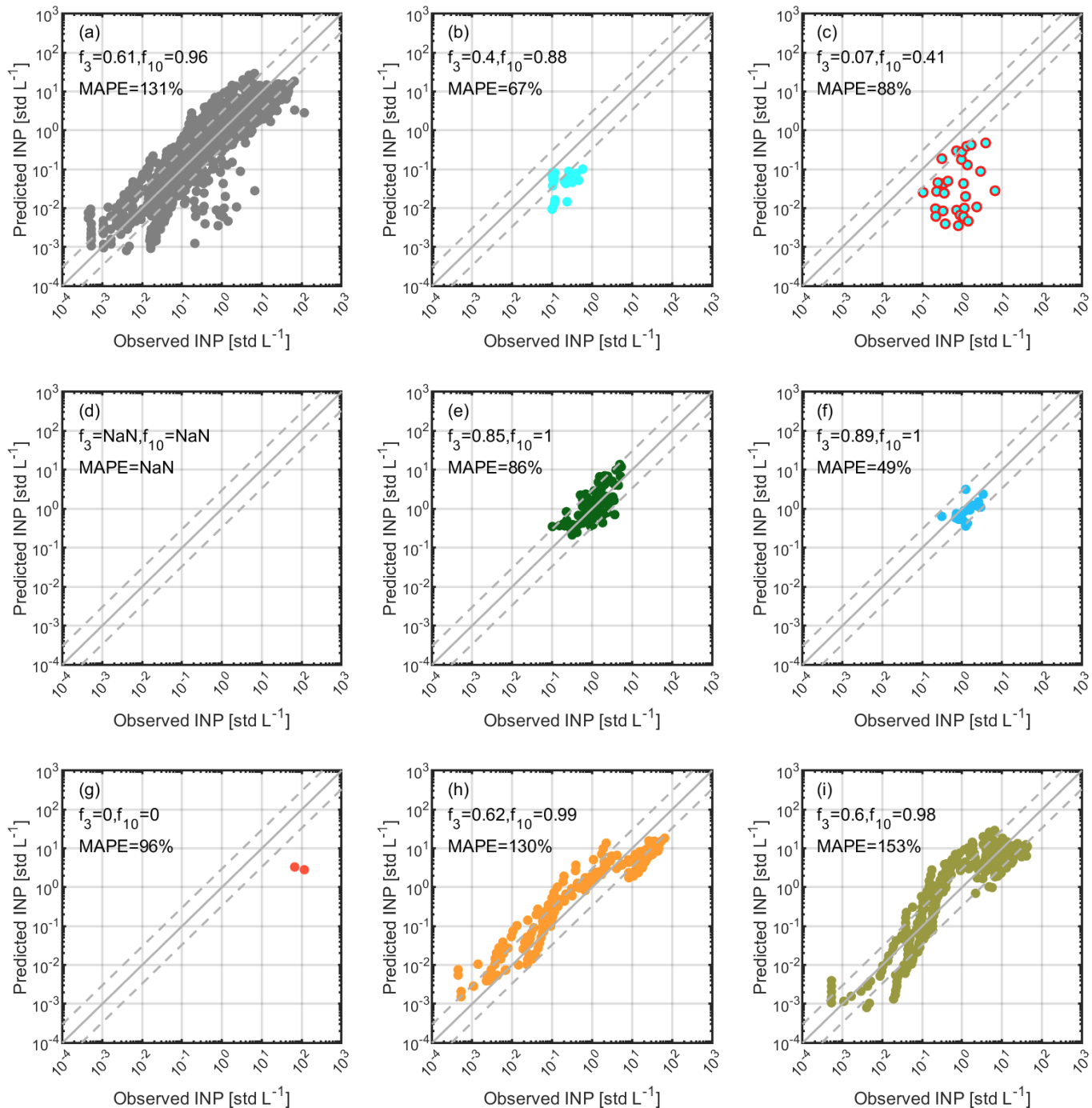


**Figure S20** The same as Fig. S14 but for evaluating the predictability of Helmos DeMott2015. Note that the sum of sub-datasets from panel (b) to (i) is smaller than the dataset presented in panel (a) because INP source apportionment is not available for all observations.

245

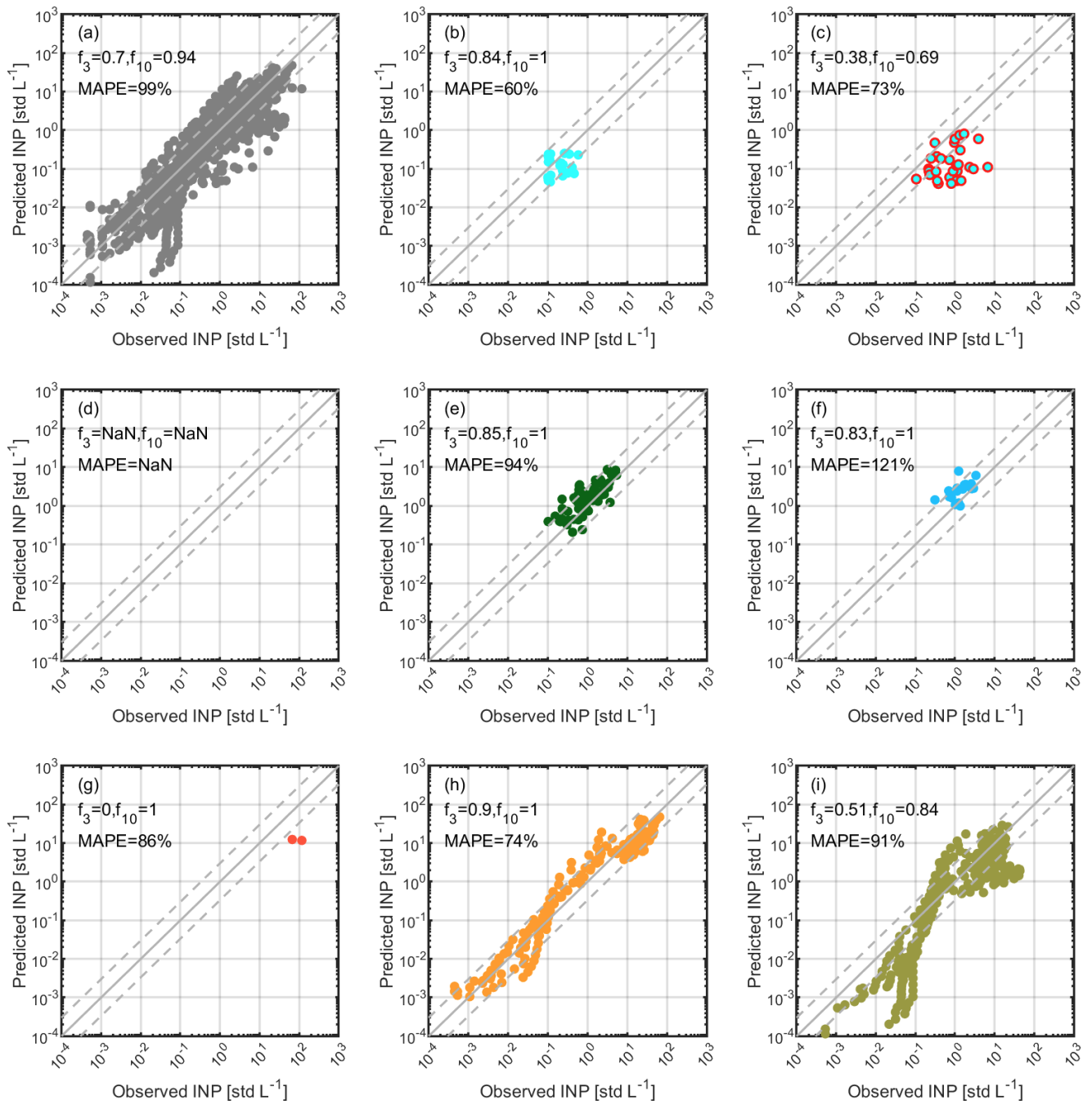
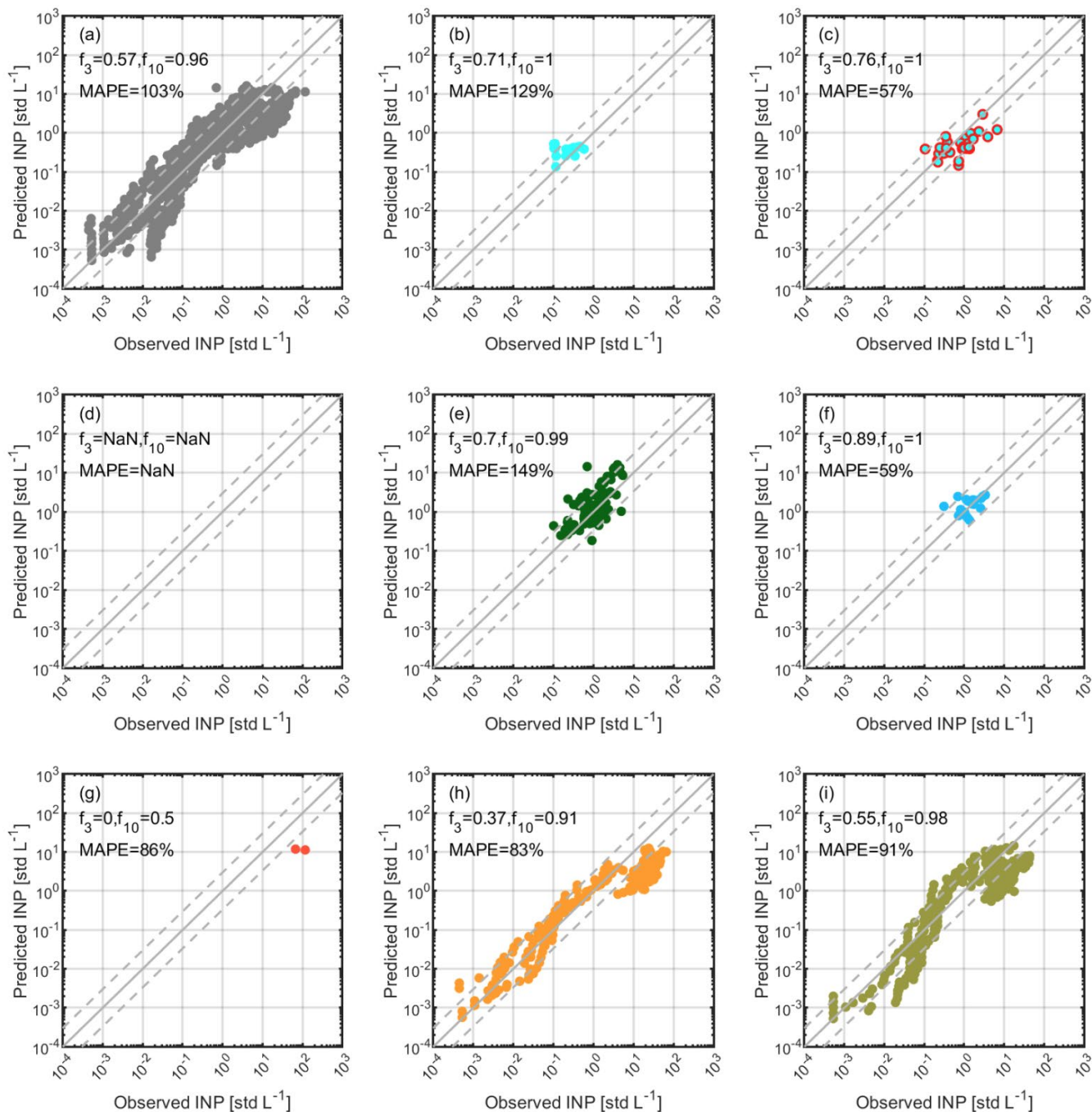


**Figure S21.** The same as Fig. S14 but for evaluating the predictability of Helmos Total<sub>APS</sub>. Note that the sum of sub-datasets from panel (b) to (i) is smaller than the dataset presented in panel (a) because INP source apportionment is not available for all observations.



255 **Figure S22.** The same as Fig. S14 but for evaluating the predictability of Helmos Tobo2013FBAP. Note that the sum of sub-datasets from panel (b) to (i) is smaller than the dataset presented in panel (a) because INP source apportionment is not available for all observations.

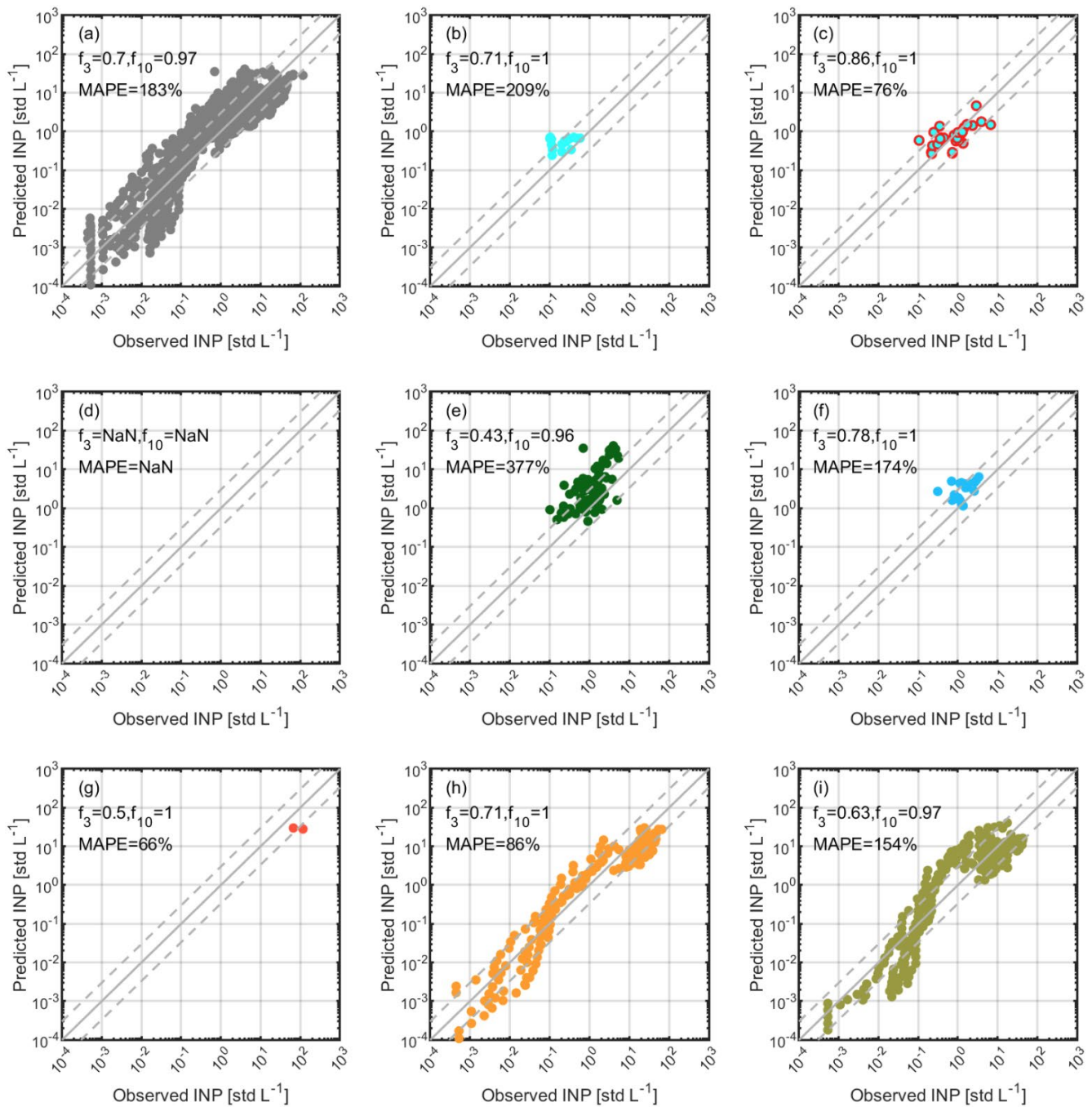


**Figure S23.** The same as Fig. S14 but for evaluating the predictability of Helmos FluowIBS. Note that the sum of sub-datasets from panel (b) to (i) is smaller than the dataset presented in panel (a) because INP source apportionment is not available for all observations.

260

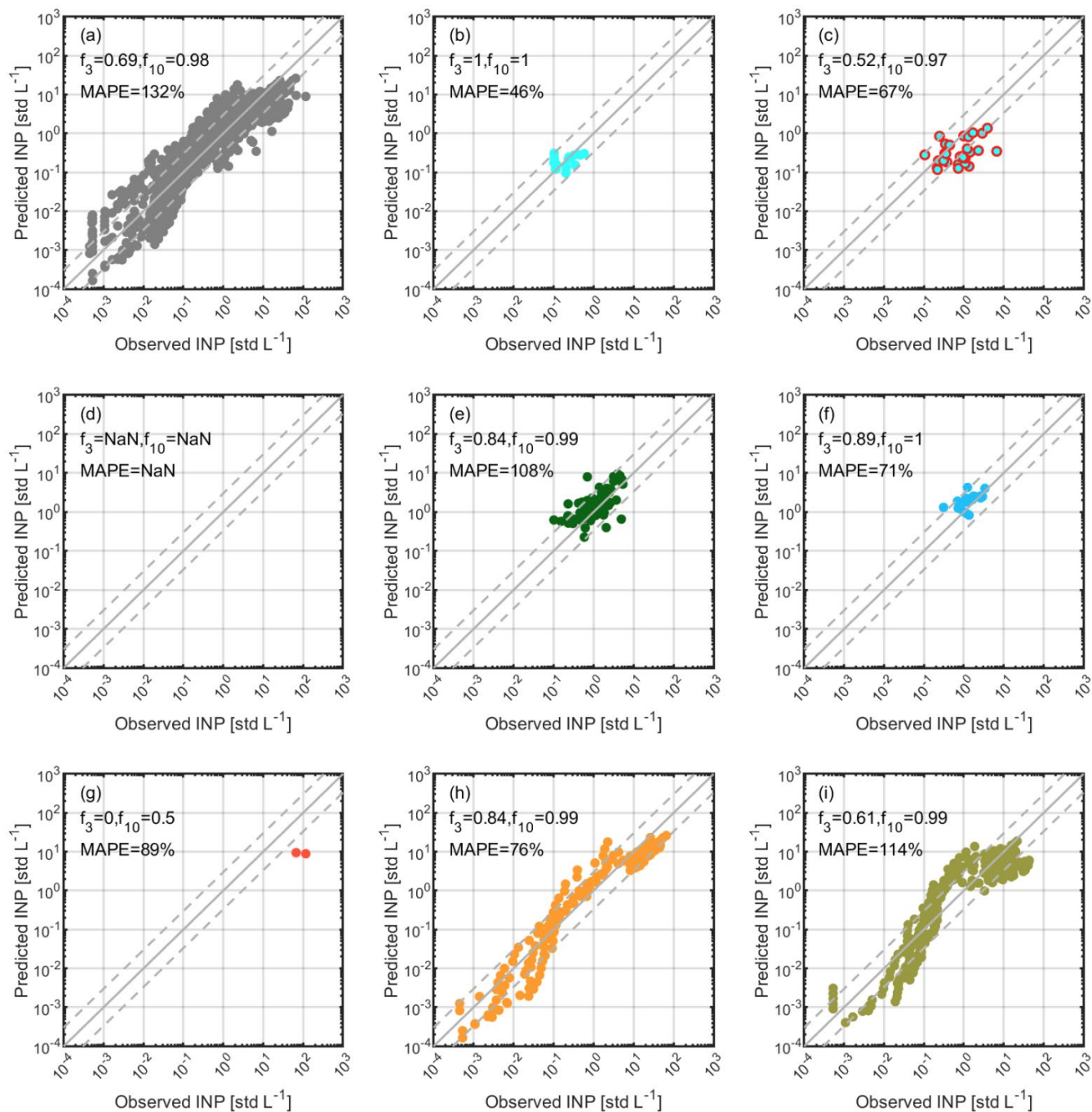


**Figure S24.** The same as Fig. S14 but for evaluating the predictability of Helmos Total<sub>WIBS\_1</sub>. Note that the sum of sub-datasets from panel (b) to (i) is smaller than the dataset presented in panel (a) because INP source apportionment is not available for all observations.

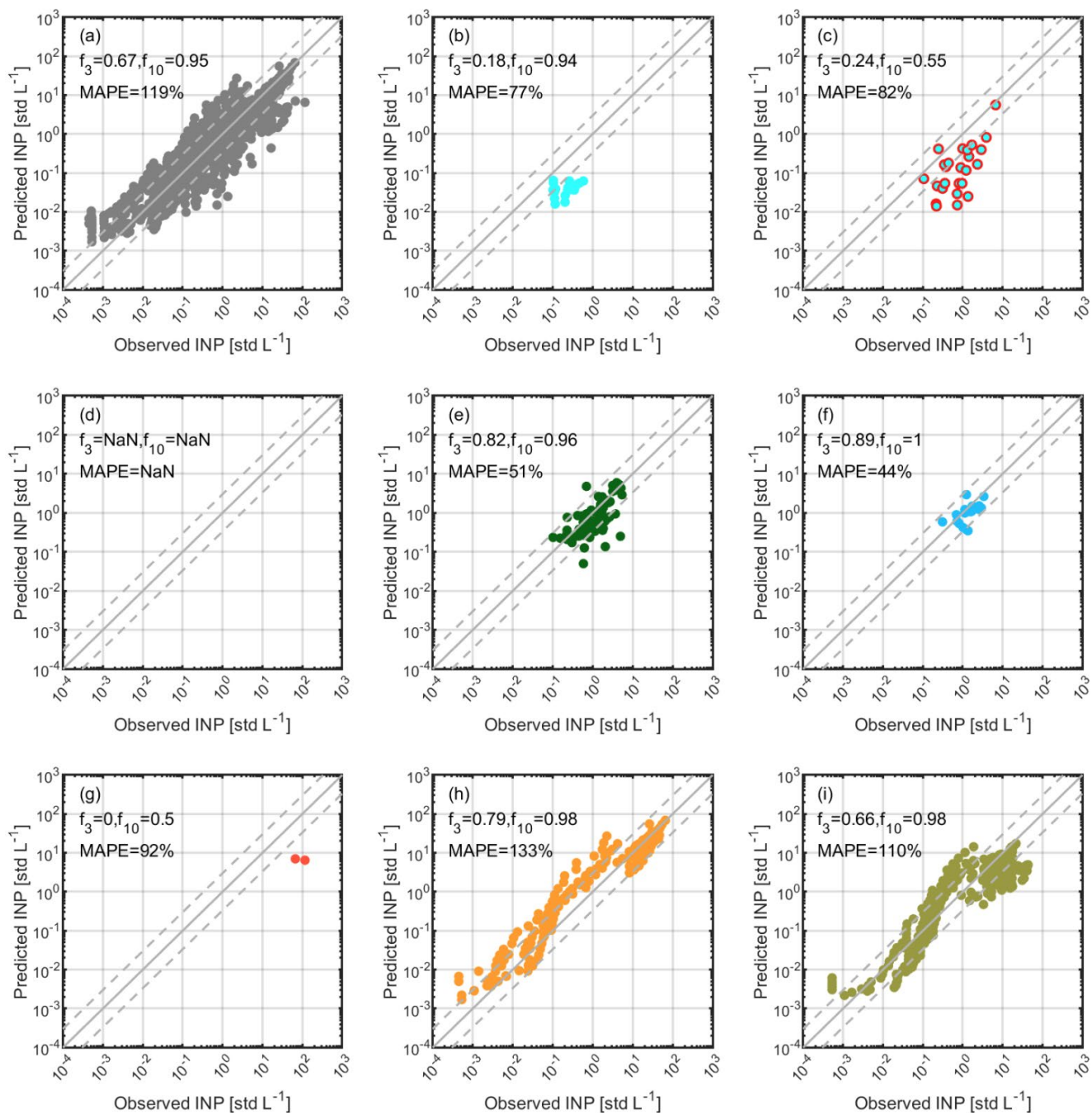


**Figure S25.** The same as Fig. S14 but for evaluating the predictability of Helmos Total<sub>WIBS\_2</sub>. Note that the sum of sub-datasets from panel (b) to (i) is smaller than the dataset presented in panel (a) because INP source apportionment is not available for all observations.

### **S11 The predictability of INP parameterizations using both SMPS and APS data**

275 Figures S26 to S28 show the performance of INP parameterizations using both SMPS and APS data for predicting  $N_{\text{INP}}$  in  
different aerosol sources. Compared to Helmos Total<sub>SMPS+APS\_1</sub> parameterization in Fig. S26, the use of SMPS\_APS<sub>Ratio</sub> in  
Helmos Total<sub>SMPS+APS\_2</sub> parameterization generally improves the predictability for INPs in dust containing aerosol sources.  
Figure S28 shows that Helmos S<sub>SMPS+APS</sub> can predict more than 90% of INPs from different sources within a factor of 10  
compared to observed data. The lower predictability for INPs from the source of South dust in PBL after marine aerosols may  
be due to the short observations (Fig. S28g). Note that the source apportionment for INSEKT INPs was conducted only when  
280 the whole INSEKT filter sampling period fitted in a period of classified aerosol source.

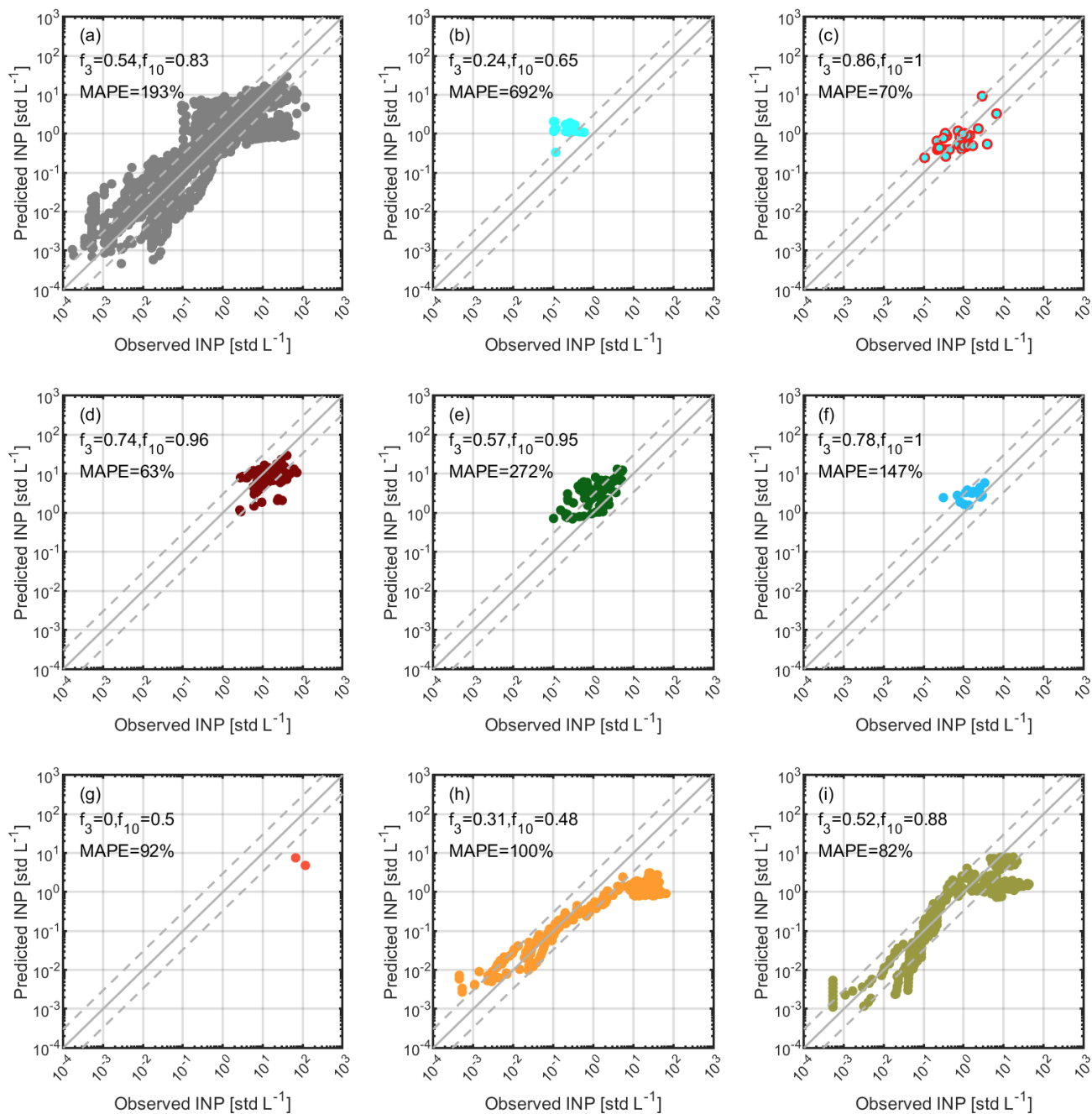
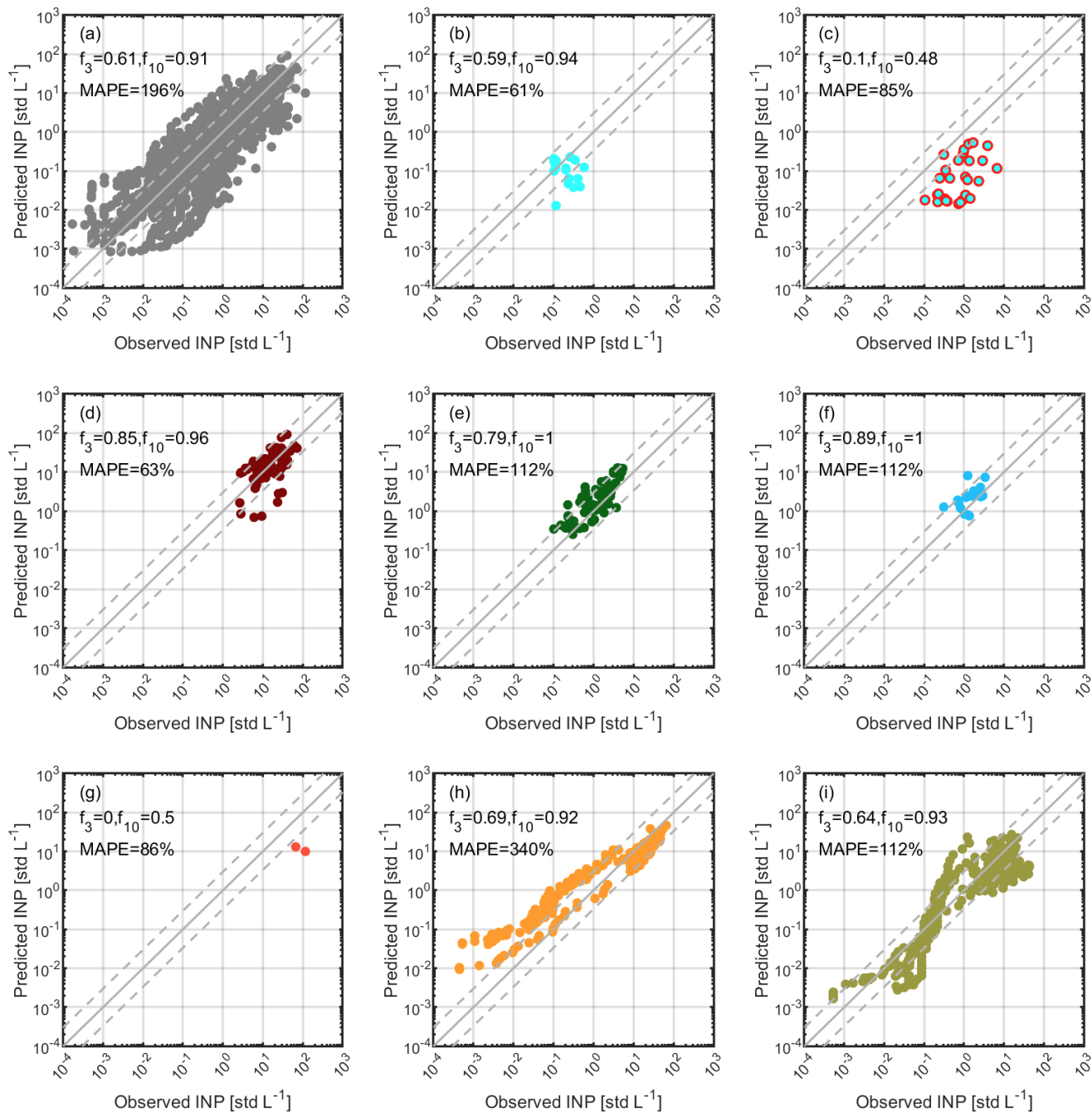


**Figure S26.** The predictability of Helmos Totals<sub>SMPS+APS\_1</sub> for INPs observed at (HAC)<sup>2</sup> from different sources when both SMPS and APS data are available. (a) All observations when both APS and SMPS data are available. (b) (HAC)<sup>2</sup> in FT under background condition. (c) (HAC)<sup>2</sup> in FT with precipitation/clouds. (d) North continental aerosols in PBL. No WIBS data. (e) North continental aerosols above PBL. (f) Marine aerosols above PBL. (g) South dust in PBL after marine aerosols. (h) South dust in PBL. (i) South dust with North continental aerosols. Note that the sum of sub-datasets from panel (b) to (i) is smaller than the dataset presented in panel (a) because INP source apportionment is not available for all observations.





290

295

**Figure S27.** The predictability of Helmos Totals<sub>SMPS+APS\_2</sub> for INPs observed at (HAC)<sup>2</sup> from different sources when both SMPS and APS data are available. (a) All observations when both APS and SMPS data are available. (b) (HAC)<sup>2</sup> in FT under background condition. (c) (HAC)<sup>2</sup> in FT with precipitation/clouds. (d) North continental aerosols in PBL. No WIBS data. (e) North continental aerosols above PBL. (f) Marine aerosols above PBL. (g) South dust in PBL after marine aerosols. (h) South dust in PBL. (i) South dust with North continental aerosols. Note that the sum of sub-datasets from panel (b) to (i) is smaller than the dataset presented in panel (a) because INP source apportionment is not available for all observations.

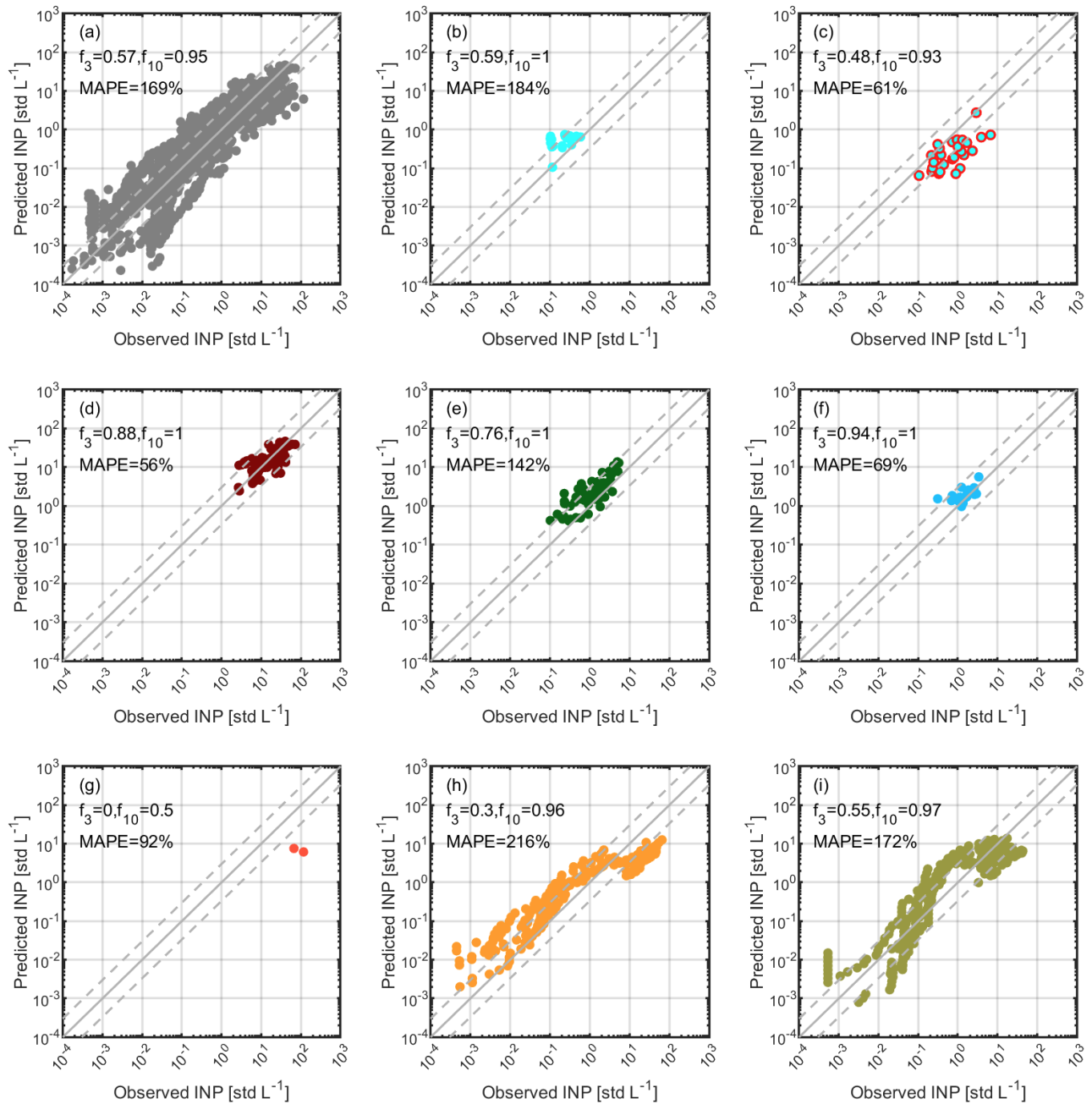
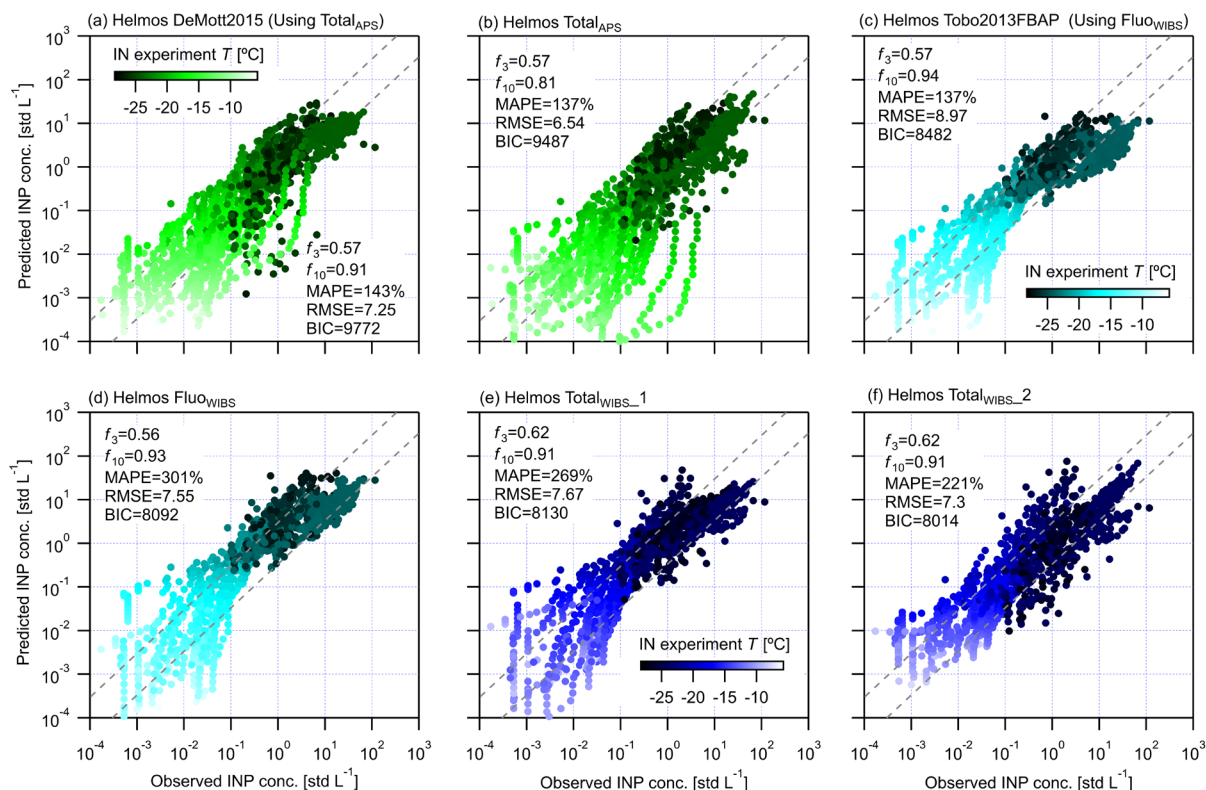


**Figure S28.** The predictability of Helmos  $S_{SMPS+APS}$  for INPs observed at  $(HAC)^2$  from different sources when both SMPS and APS data are available. (a) All observations when both APS and SMPS data are available. (b)  $(HAC)^2$  in FT under background condition. (c)  $(HAC)^2$  in FT with precipitation/clouds. (d) North continental aerosols in PBL. No WIBS data. (e) North continental aerosols above PBL. (f) Marine aerosols above PBL. (g) South dust in PBL after marine aerosols. (h) South dust in PBL. (i) South dust with North continental aerosols. Note that the sum of sub-datasets from panel (b) to (i) is smaller than the dataset presented in panel (a) because INP source apportionment is not available for all observations.

300

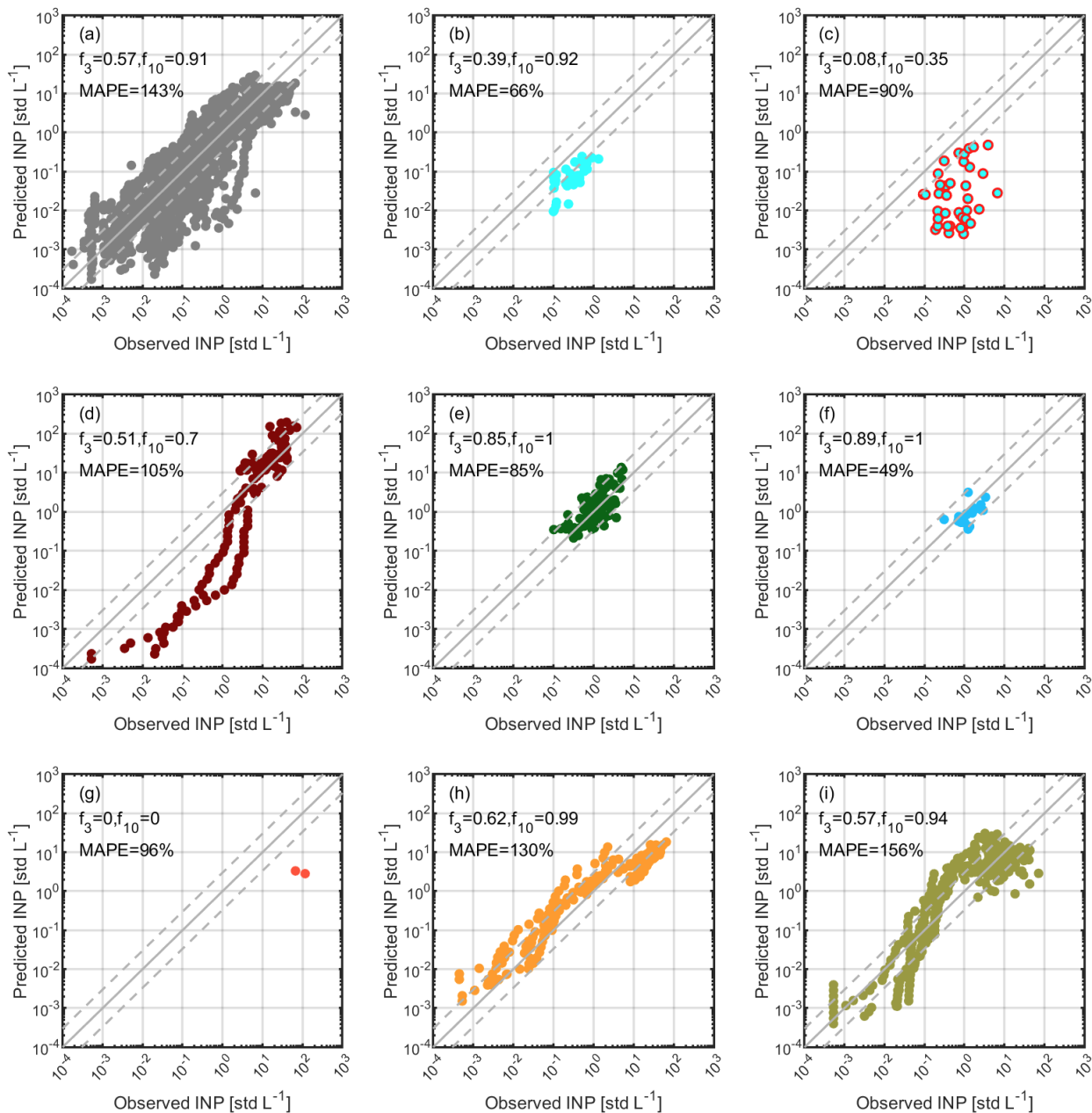
305 **S12 The predictability of INP parameterization methods proposed in this study for INPs originated from different sources for all observations when APS or WIBS data are available**

Figure S29 shows an overview of the predictability of different parameterizations to predict INPs for observation periods when APS or WIBS data are available. Helmos DeMott2015 and Helmos Total<sub>APS</sub> are used to calculate  $N_{INP}$  for periods when APS data are available which is a dataset larger than the training dataset by 40%. The parameterizations based on WIBS particle  
 310 properties are also evaluated to test a larger dataset by 1.2 times compared to training dataset. Figures S30 to S35 show the predictability of individual parameterizations to predict INPs from different sources. Note that the lower predictability for INPs from the source of South dust in PBL after marine aerosols may be due to the very limited observations (< 3 hours). Also, the source apportionment for INSEKT INPs was conducted only when the whole INSEKT filter sampling period fitted in a period of classified aerosol source.



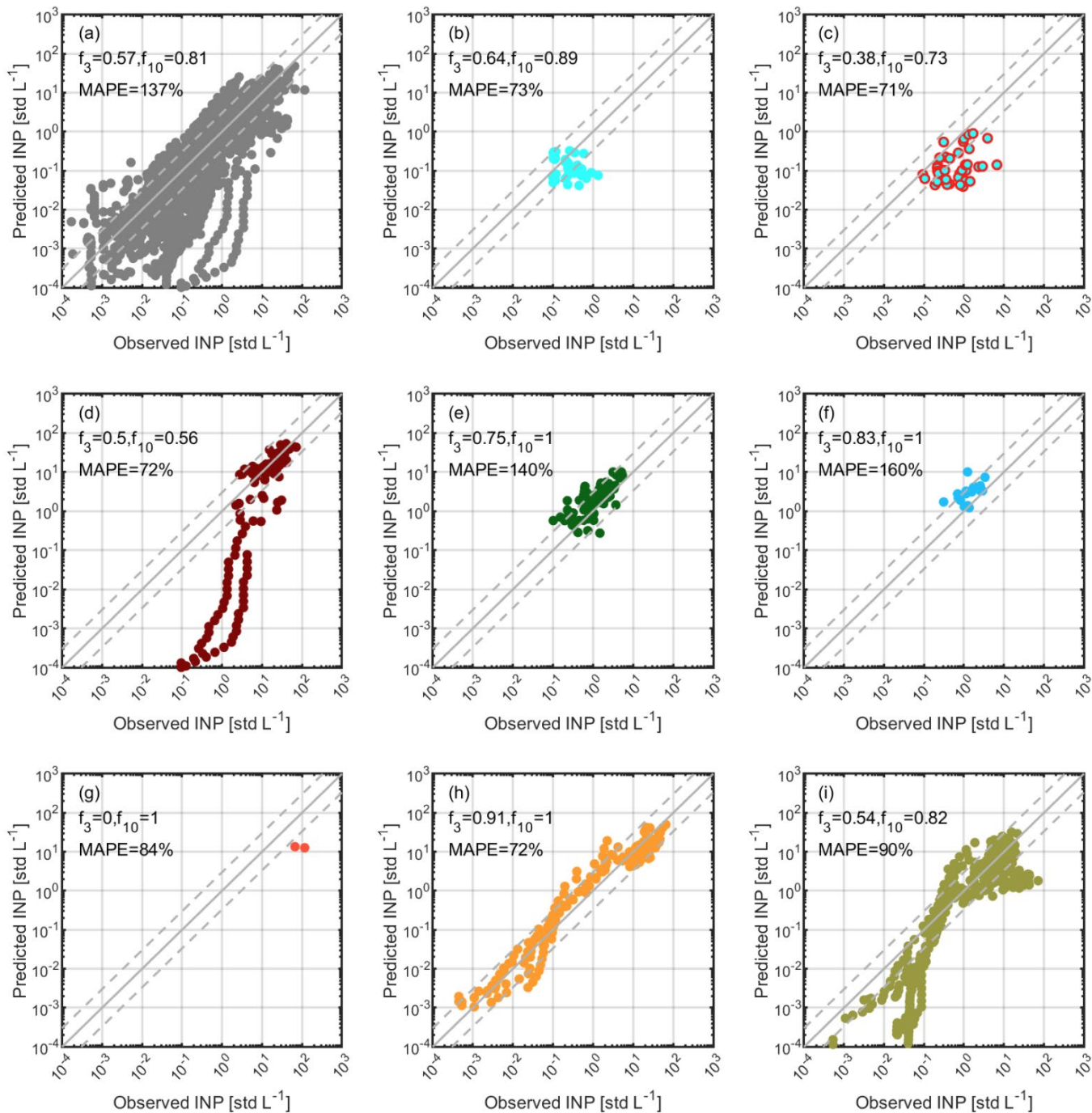
315 **Figure S29. The predictability of different parameterization methods for all INPs observed at (HAC)<sup>2</sup> when APS (panel a and b) or WISB (panel c, d, e and f) data are available. (a) Helmos DeMott2015. (b) Helmos Total<sub>APS</sub>. (c) Helmos Tobo2013FBAP. (d) Helmos Fluo<sub>WIBS</sub>. (e) Helmos Total<sub>WIBS\_1</sub>. (f) Helmos Total<sub>WIBS\_2</sub>. The IN experiment temperature for observed INP data points is scaled to the colour bar. Note that parameterizations using the same aerosol properties use the same color bar. The dashed lines confine the range for observed and predicted data points within a factor of 3. The fraction of observed and predicted data points within a factor of 3 ( $f_3$ ) and 10 ( $f_{10}$ ) is provided in each panel, respectively. MAPE stands for mean absolute percentage error. The results are based on observations for periods when both APS and WIBS are available, thus all parametrizations are based on the same dataset. RMSE is the root-mean-square error used as a measure of the difference between observed and predicted data. BIC is a value calculated by applying the Bayesian information criteria to evaluate the goodness of parameterizations based on the same dataset.**

320

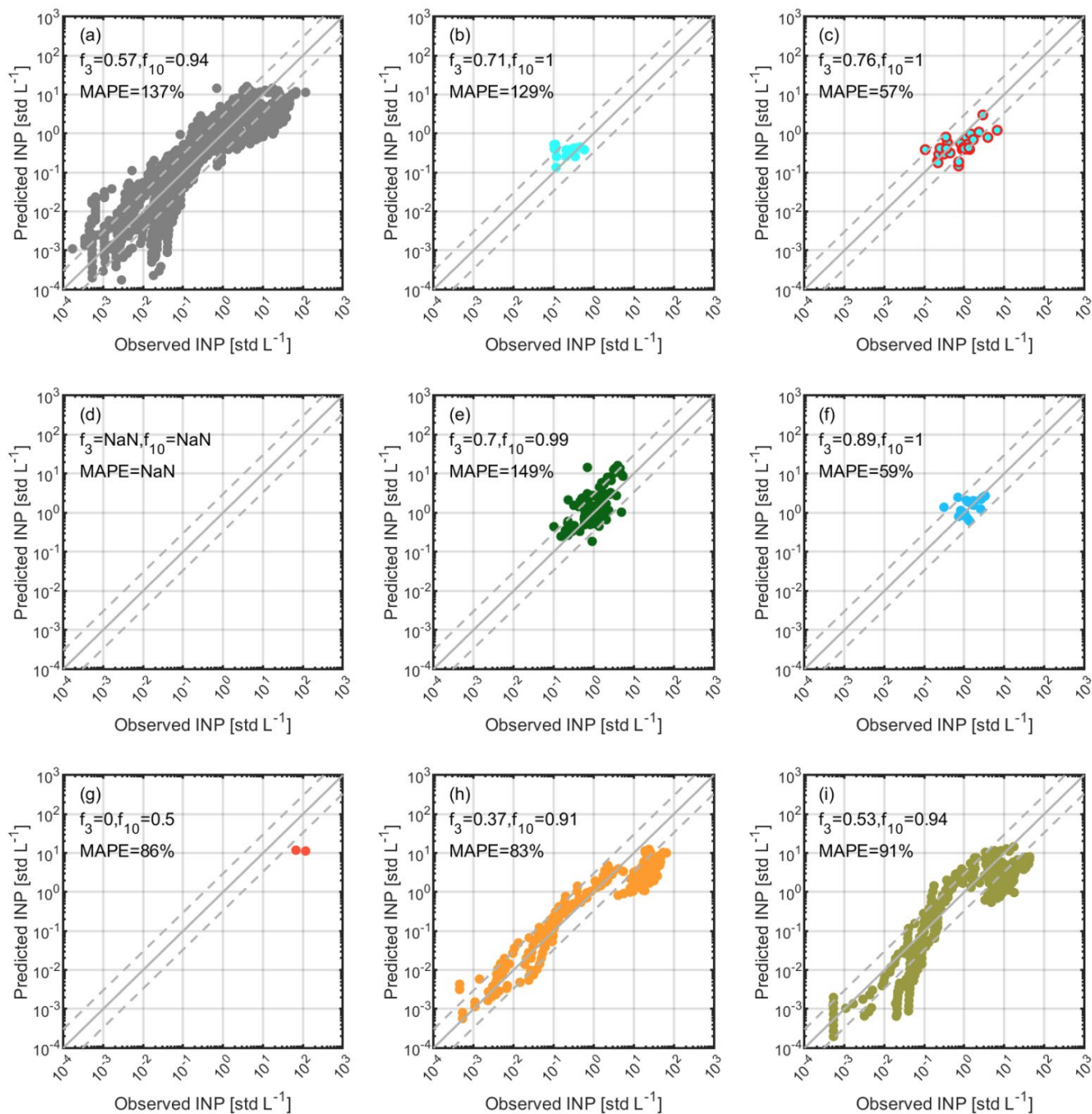


**Figure S30.** The predictability of Helmos DeMott2015 for INPs observed at  $(\text{HAC})^2$  from different sources when APS data are available. (a) All observations when both APS and WIBS data are available. (b)  $(\text{HAC})^2$  in FT under background condition. (c)  $(\text{HAC})^2$  in FT with precipitation/clouds. (d) North continental aerosols in PBL. No WIBS data. (e) North continental aerosols above PBL. (f) Marine aerosols above PBL. (g) South dust in PBL after marine aerosols. (h) South dust in PBL. (i) South dust with North continental aerosols. Note that the sum of sub-datasets from panel (b) to (i) is smaller than the dataset presented in panel (a) because INP source apportionment is not available for all observations.

330



335 **Figure S31.** The same as Fig. S30 but for evaluating the predictability of Helmos Total<sub>APS</sub>. Note that the sum of sub-datasets from panel (b) to (i) is smaller than the dataset presented in panel (a) because INP source apportionment is not available for all observations.



340 **Figure S32.** The predictability of Helmos Tobo2013FBAP for INPs observed at  $(\text{HAC})^2$  from different sources when WIBS data are  
 345 available. (a) All observations when both APS and WIBS data are available. (b)  $(\text{HAC})^2$  in FT under background condition. (c)  
 $(\text{HAC})^2$  in FT with precipitation/clouds. (d) North continental aerosols in PBL. No WIBS data. (e) North continental aerosols above  
 PBL. (f) Marine aerosols above PBL. (g) South dust in PBL after marine aerosols. (h) South dust in PBL. (i) South dust with North  
 continental aerosols. Note that the sum of sub-datasets from panel (b) to (i) is smaller than the dataset presented in panel (a) because  
 INP source apportionment is not available for all observations.

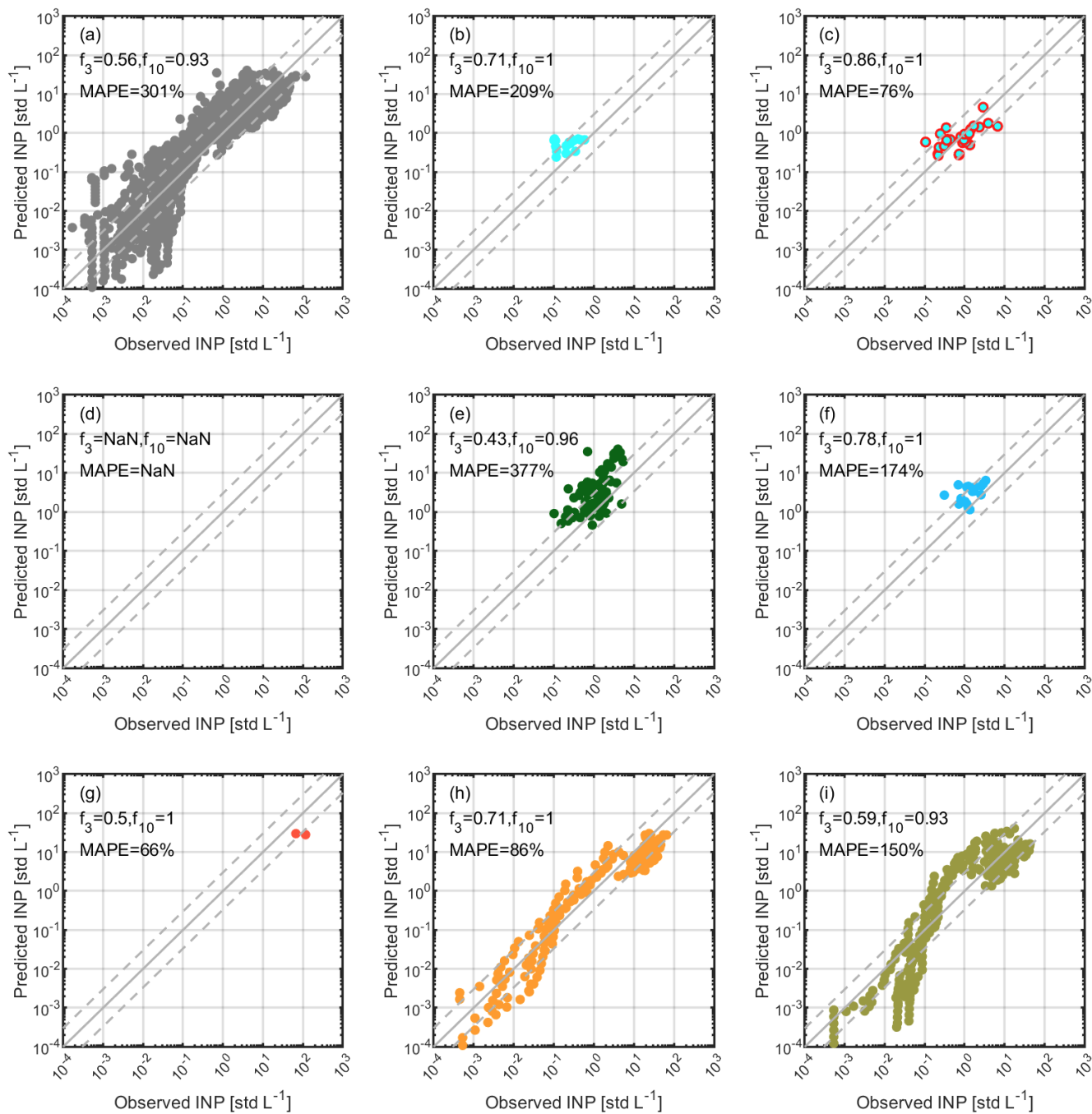


**Figure S33.** The same as Fig. S32 but for evaluating the predictability of Helmos Fluowibs. Note that the sum of sub-datasets from panel (b) to (i) is smaller than the dataset presented in panel (a) because INP source apportionment is not available for all observations.

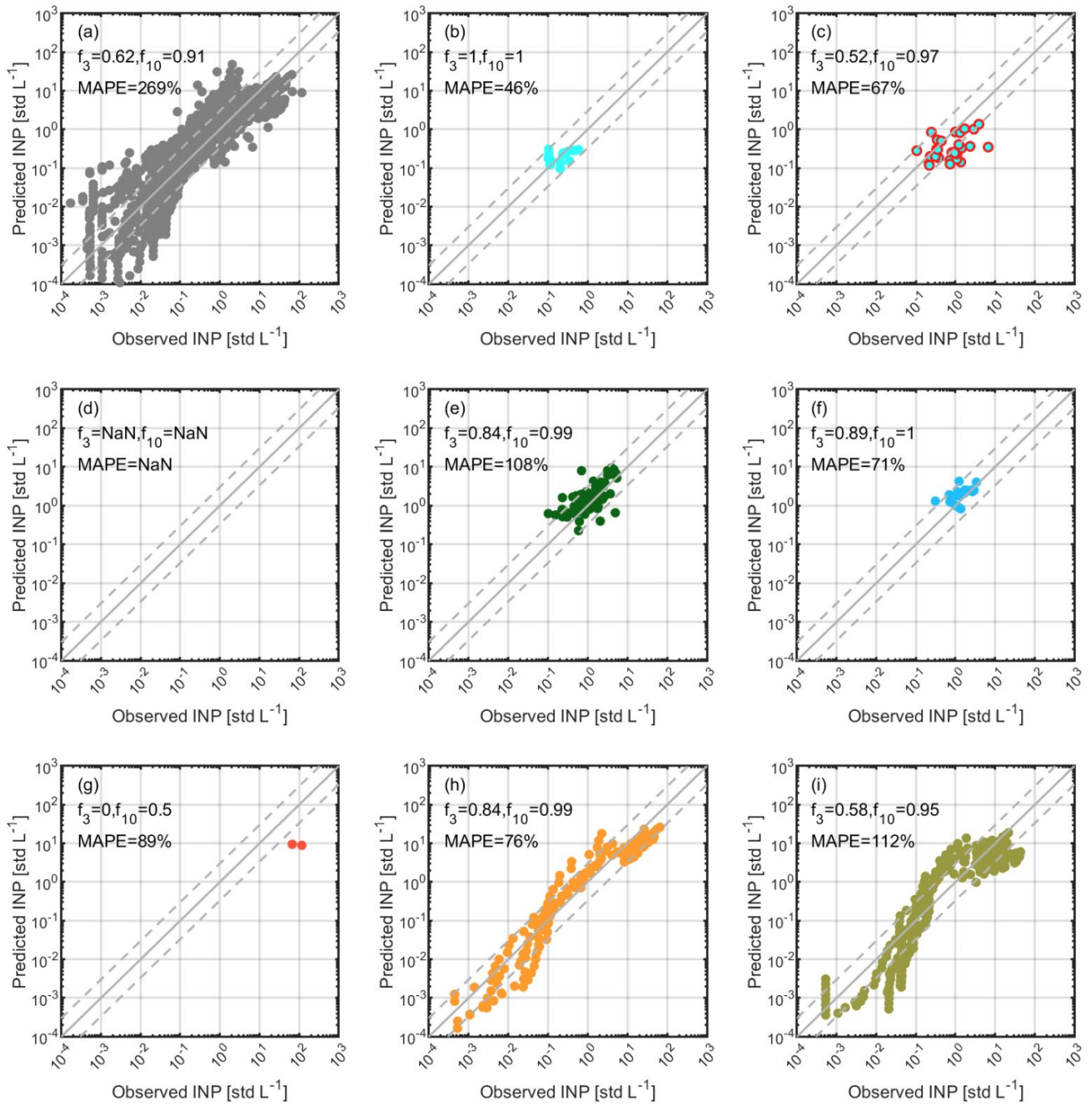


**Figure S34.** The same as Fig. S32 but for evaluating the predictability of Helmos Total<sub>WBS\_1</sub>. Note that the sum of sub-datasets from panel (b) to (i) is smaller than the dataset presented in panel (a) because INP source apportionment is not available for all observations.



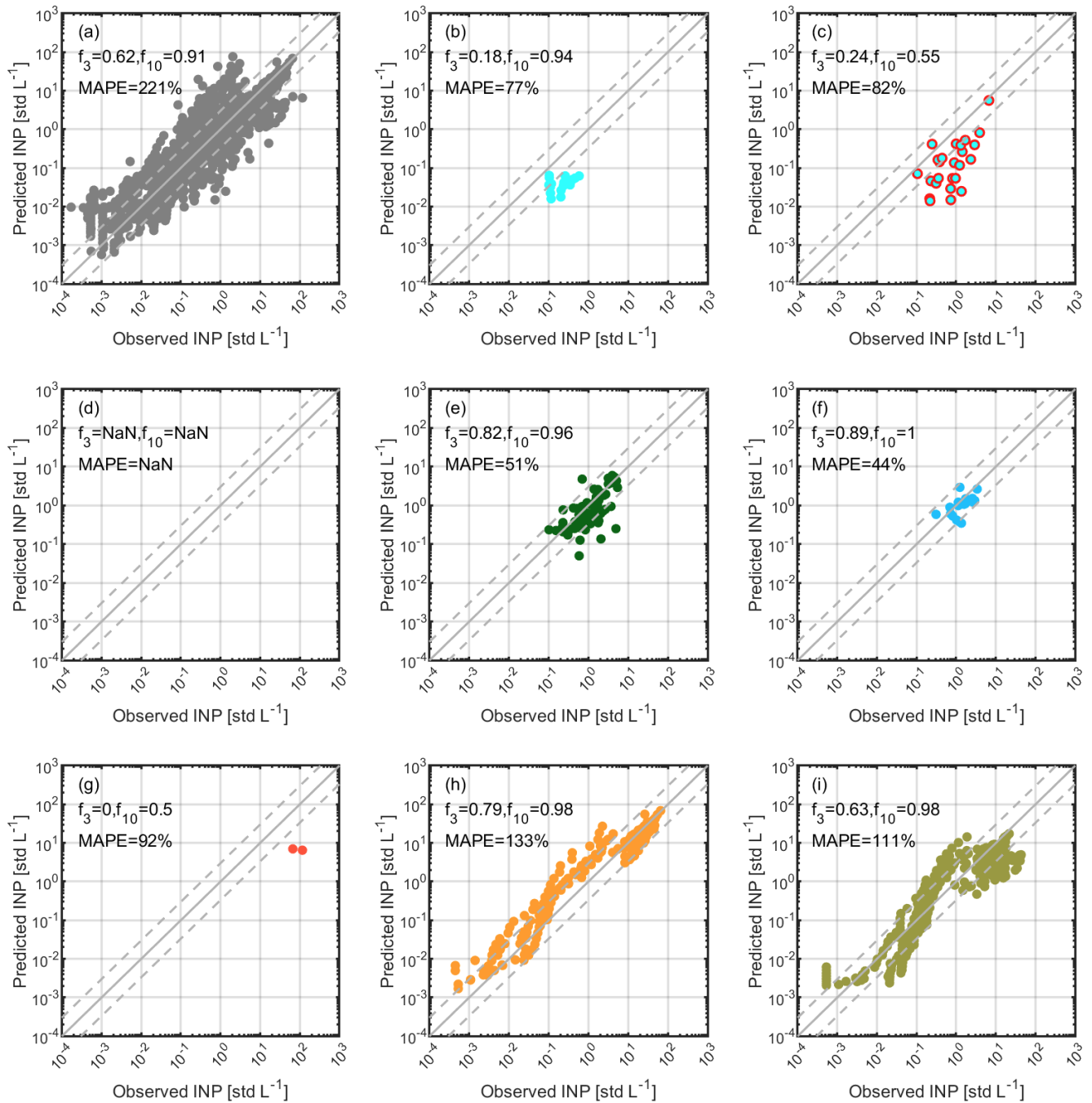


**Figure S35.** The same as Fig. S32 but for evaluating the predictability of Helmos Total<sub>WIBS\_2</sub>. Note that the sum of sub-datasets from panel (b) to (i) is smaller than the dataset presented in panel (a) because INP source apportionment is not available for all observations.

## References

- Barry, K. R., Hill, T. C. J., Levin, E. J. T., Twohy, C. H., Moore, K. A., Weller, Z. D., Toohey, D. W., Reeves, M., Campos, T., Geiss, R., Schill, G. P., Fischer, E. V., Kreidenweis, S. M., and DeMott, P. J.: Observations of Ice Nucleating Particles in the Free Troposphere From Western US Wildfires, *J. Geophys. Res. Atmos.*, 126, <https://doi.org/10.1029/2020jd033752>, 2021.
- 365 Brunner, C., Brem, B. T., Collaud Coen, M., Conen, F., Hervo, M., Henne, S., Steinbacher, M., Gysel-Beer, M., and Kanji, Z. A.: The contribution of Saharan dust to the ice-nucleating particle concentrations at the High Altitude Station Jungfraujoch (3580 m a.s.l.), Switzerland, *Atmos. Chem. Phys.*, 21, 18029-18053, <https://doi.org/10.5194/acp-21-18029-2021>, 2021.
- Khan, B., Stenchikov, G., Weinzierl, B., Kalenderski, S., and Osipov, S.: Dust plume formation in the free troposphere and aerosol size distribution during the Saharan Mineral Dust Experiment in North Africa, *Tellus B Chem. Phys. Meteorol.*, 67, 370 <https://doi.org/10.3402/tellusb.v67.27170>, 2015.
- Khlystov, A., Stanier, C., and Pandis, S. N.: An Algorithm for Combining Electrical Mobility and Aerodynamic Size Distributions Data when Measuring Ambient Aerosol Special Issue of Aerosol Science and Technology on Findings from the Fine Particulate Matter Supersites Program, *Aerosol Sci. Technol.*, 38, 229-238, <https://doi.org/10.1080/02786820390229543>, 2004.
- 375 Li, G., Wieder, J., Pasquier, J. T., Henneberger, J., and Kanji, Z. A.: Predicting atmospheric background number concentration of ice nucleating particles in the Arctic, *Atmospheric Chemistry and Physics Discussions*, <https://doi.org/10.5194/acp-2022-21>, 2022.